Article

Cell Systems

Compact transcription factor cassettes generate functional, engraftable motor neurons by direct conversion

Graphical abstract

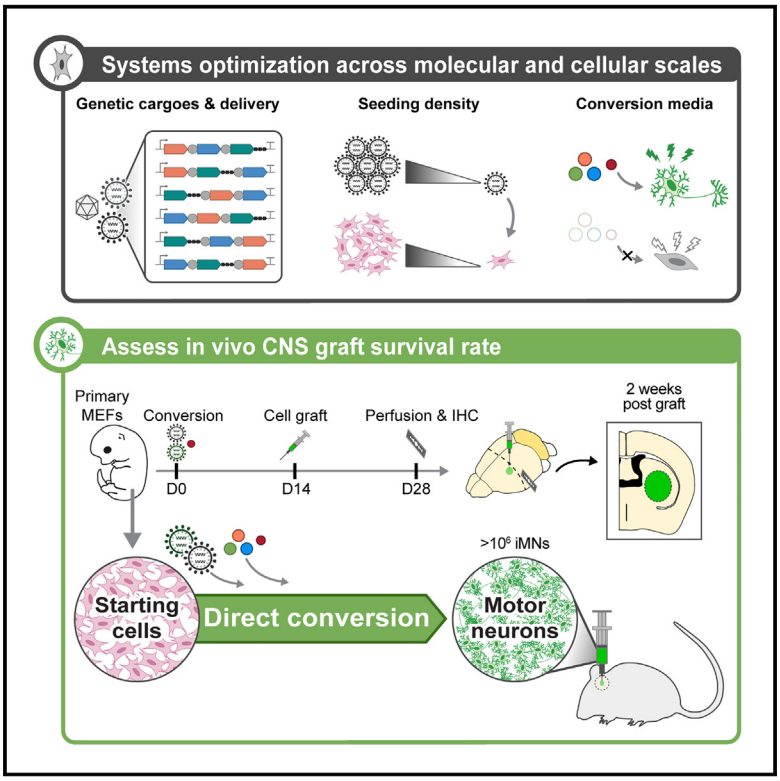

Highlights

- Compact, conversion cassettes are compatible with diverse delivery vectors
- Cocktail and conversion culture conditions influence the cell states of iMNs
- Optimized conversion cocktail supports neurotrophin-free conversion to iMN-like cells
- iMNs display electrical activity and graft *in vivo* within the central nervous system

Authors

Nathan B. Wang, Honour O. Adewumi, Brittany A. Lende-Dorn, Adam M. Beitz, Timothy M. O'Shea, Kate E. Galloway

Correspondence

katiegal@mit.edu

In brief

Wang et al. develop compact conversion cassettes to massively increase the rates of direct conversion to induced motor neurons, generating functional, engraftable motor neurons from easily accessible fibroblasts.

Wang et al., 2025, Cell Systems *16*, 101206
April 16, 2025
https://doi.org/10.1016/j.cels.2025.101206

CellPress

Cell Systems

CellPress

Article

Compact transcription factor cassettes generate functional, engraftable motor neurons by direct conversion

Nathan B. Wang,[1] Honour O. Adewumi,[2] Brittany A. Lende-Dorn,[1] Adam M. Beitz,[1] Timothy M. O'Shea,[2] and Kate E. Galloway[1,3,*]

[1]Department of Chemical Engineering, Massachusetts Institute of Technology, Cambridge, MA 02139, USA
[2]Department of Biomedical Engineering, Boston University, Boston, MA 02215, USA
[3]Lead contact
*Correspondence: katiegal@mit.edu
https://doi.org/10.1016/j.cels.2025.101206

SUMMARY

Direct conversion generates patient-specific, disease-relevant cell types, such as neurons, that are rare, limited, or difficult to isolate from common and easily accessible cells, such as skin cells. However, low rates of direct conversion and complex protocols limit scalability and, thus, the potential of cell-fate conversion for biomedical applications. Here, we optimize the conversion protocol by examining process parameters, including transcript design; delivery via adeno-associated virus (AAV), retrovirus, and lentivirus; cell seeding density; and the impact of media conditions. Thus, we report a compact, portable conversion process that boosts proliferation and increases direct conversion of mouse fibroblasts to induced motor neurons (iMNs) to achieve high conversion rates of above 1,000%, corresponding to more than ten motor neurons yielded per cell seeded, which we achieve through expansion. Our optimized, direct conversion process generates functional motor neurons at scales relevant for cell therapies (>10^7 cells) that graft with the mouse central nervous system. High-efficiency, compact, direct conversion systems will support scaling to patient-specific, neural cell therapies.

INTRODUCTION

Reprogramming cell fate offers a powerful method to generate rare or inaccessible cells, such as neurons, for patient-specific disease modeling and cell replacement therapies to regenerate tissues.[1,2] Direct conversion, also called transdifferentiation, represents a subset of reprogramming protocols that convert cells from one stable somatic identity to another. Direct conversion bypasses the pluripotent stage, shortening the time required to generate neurons. Additionally, unlike in induced pluripotent stem cell (iPSC)-derived neurons, directly converted neurons can retain signatures of aging. Retention of age-related features such as epigenetic marks may improve the fidelity of *in vitro* models for age-related diseases.[3–6]

Beyond disease modeling, direct conversion offers a potentially rapid path for generating patient-specific neurons for autologous cell therapies. Cell transplantation to promote neural regeneration holds great promise to restore neurological functions. Diverse cell sources have been explored for neural replacement therapy in central nervous system (CNS) injuries to replace damaged neural tissue, reconstruct and reconnect lost neural circuits, and restore neurological functions.[7–11] Many different types of cells have been explored for CNS injury transplantation, including fetal cell grafts,[12–17] neural stem or progenitor cells (NPCs),[18–20] olfactory ensheathing cells (OECs),[21] Schwann cells,[22] various bone marrow-derived cells,[23–25] and progenitors or specialized neurons and glia derived from lines of embryonic stem cells (ESCs) or iPSCs.[26–32] The neurogenic potential of NPCs makes them an attractive cell source for generating new neurons for direct functional regeneration.[27,33,34] However, while multipotent NPC grafts provide notable benefits, there remain ethical and practical challenges for clinical translation of NPC for neural replacement therapy, including the sourcing of primary NPCs at scale, the inherent cellular heterogeneity of primary cells, and the lack of control over differentiation, localization, and function.[35–39]

Alternatively, fate-restricted neuronal grafts may provide a defined cell source that overcomes the issues of uncontrolled neurogenic potential observed in NPC grafts. However, rapidly sourcing, deriving, and purifying sufficient numbers primary- or iPSC-derived neurons for a neuronal graft presents a substantial challenge. By bypassing the intermediate pluripotent reprogramming step, direct conversion more quickly generates therapeutically relevant, autologous cells from readily accessible patient cells such as those from a skin biopsy. Rapid sourcing of therapeutic cells for delivery within the short therapeutic window is critical to support optimal recovery.[33,40] While direct conversion offers speed, realizing the potential of direct conversion requires processes that generate functional neurons at scale.

Please cite this article in press as: Wang et al., Compact transcription factor cassettes generate functional, engraftable motor neurons by direct conversion, Cell Systems (2025), https://doi.org/10.1016/j.cels.2025.101206

Engineering primary, patient-derived cells imposes substantial design restrictions that impede the translation of biological insights into manufacturing scale up. For effective scale up for cell therapies, direct conversion processes should generate functional neurons by methods that are robust to inherent process variability, such as cell culture conditions. While abundant progress has been made in identifying how cells transit through different cell fates,[41–44] translating these findings into scalable direct conversion processes for cell therapy manufacturing remains challenging. Viruses efficiently deliver transgenes to primary cells, resulting in high transgene expression. However, the packaging limits of viruses constrain cargo size and components. Optimizing transgenic cargoes for compact encoding facilitates viral packaging and minimizes extrinsic variability in the conversion process.[45,46] Compact cassettes can be easily integrated into synthetic biology tools for precise control of transcripts, such as synthetic promoter systems. Synthetic and pathway-responsive promoters and genetic circuits can readily control the transcription of a single, polycistronic cassette.[47,48] In theory, these tools can be used to guide cells through the reprogramming process to drive cell-fate conversion.[49,50] Further, in practical terms, reducing transgenic cargoes to minimal components reduces the amount of input material that must be produced, lowering the cost and complexity for manufacturing.

In this work, we set out to develop a robust, scalable, direct conversion process to generate functional motor neurons for neural cell therapies (Figure 1). Leveraging our work to examine how proliferation history and transcription factor levels combine to drive direct conversion, we designed optimized, compact conversion systems for direct conversion of primary mouse embryonic fibroblasts (MEFs) to motor neurons. We compared conversion rates from the standard retroviral transduction to conversion with clinically relevant viral transduction using adeno-associated virus (AAV) and inducible lentivirus for transcriptional control. Additionally, we explored additional process features with our minimal vector systems to improve manufacturing while retaining functional features. To demonstrate the potential for future translational applications, we generated motor neuron grafts from fibroblasts that can integrate with the mouse CNS. Overall, our work offers a roadmap for the translation of mechanistic insights into the optimization of molecular and process features of direct conversion to generate functional, engraftable neurons by direct conversion at scales sufficient for cell therapies.

RESULTS

Optimized, compact, single-transcript conversion cassettes increase conversion rates

Compact cassettes of transcription factors ease size-imposed design constraints. Smaller cassettes also support portability to a range of vectors for comparison and control of transgene expression in primary cells. Previously, we identified a minimal chemogenetic cocktail for highly efficient direct conversion of MEFs to induced motor neurons (iMNs) composed of two modules: a motor neuron conversion module and a high-efficiency module.[46] The conversion module is composed of a minimal set of three transcription factors for motor neuron conversion: Ngn2, a pioneer transcription factor, and Isl1 and Lhx3, two motor neuron-specific factors. The high-efficiency module, termed DDRR (DDRR: p53DD [DD], HRAS^{G12V} [R], and the small-molecule transforming growth factor β (TGF-β)-inhibitor RepSox [R]) is a chemogenetic cocktail with oncogenic (p53DD and HRAS^{G12V}) and chemical components (RepSox). DDRR boosts direct conversion by supporting hyperproliferative cells while reducing genomic stress through topoisomerase activation.[51] We delivered the conversion factors encoded on retroviruses to transgenic MEFs bearing the motor neuron reporter, Hb9::GFP,[52] which allows us to monitor conversion dynamically. Activation of Hb9::GFP and neuronal morphology provide live metrics of the conversion process.[46] Importantly, each fully converted iMN corresponds to exactly one conversion event, allowing us to quantitatively evaluate how perturbations impact the number of successful events.

To allow for simple, uniform transcriptional control and to decrease the number of genetic cargoes required for co-delivery, we first aimed to identify the optimal single-transcript encoding for each module (Figure 2A). The motor neuron conversion module includes three transcription factors (Ngn2, Isl1, and Lhx3), and the genetic portion of the high-efficiency module has two additional transgenes (p53DD and HRAS^{G12V}). Putatively, the ordering of genes on a single-transcript influences gene expression. Genes at upstream positions are expected to be translated at greater frequencies than at downstream positions.[53] However, relative levels of expression from polycistronic cassettes are context- and encoding-dependent.[54–59] Thus, while we had identified putatively optimal profiles of exogenous expression for each of the three transcription factors,[46] we hypothesized that the ordering on a polycistronic cassette may not fully prescribe expression levels. Therefore, we sought to identify the optimal encoding by exploring all permutations of single-transcript, polycistronic cassettes. To capture multiple dimensions of the conversion process's efficiency, we quantified conversion rates using two metrics: "yield" and "purity" (Figures 2B and 2C). We quantify yield by how many converted cells are at the final time point relative to the starting cell input. Yield increases for highly proliferative conditions and measures how many successful conversion events occur from an initial seeded population. We also quantify purity by the percent of cells of the total population that are converted at that time point. Purity measures the proportion of the cells at the terminal point that have converted into the desired cell fate. Yield and purity are generally correlated; however, differences in these metrics may reflect different proliferation rates between cells, such as non-converted and converted iMNs. Yield is important for assessing how many initial cells need to be seeded to generate a specified number of converted cells, while purity is important for scaling purification steps.

We first investigated single-transcript encodings of the high-efficiency module, as we reasoned that an optimal high-efficiency module would aid in the design of the conversion module. For the conversion module, we used a single-transcript design termed NIL that we and others have already used, where each transcription factor (Ngn2, Isl1, and Lhx3) is separated by a small, "self-cleaving" 2A sequence.[46,60] We explored how the placement of p53DD and HRAS^{G12V} relative to an internal ribosome entry site (IRES) impacts the rate of conversion (Figure 2D). Overexpressing the DDRR module variants with the

Please cite this article in press as: Wang et al., Compact transcription factor cassettes generate functional, engraftable motor neurons by direct conversion, Cell Systems (2025), https://doi.org/10.1016/j.cels.2025.101206

CellPress

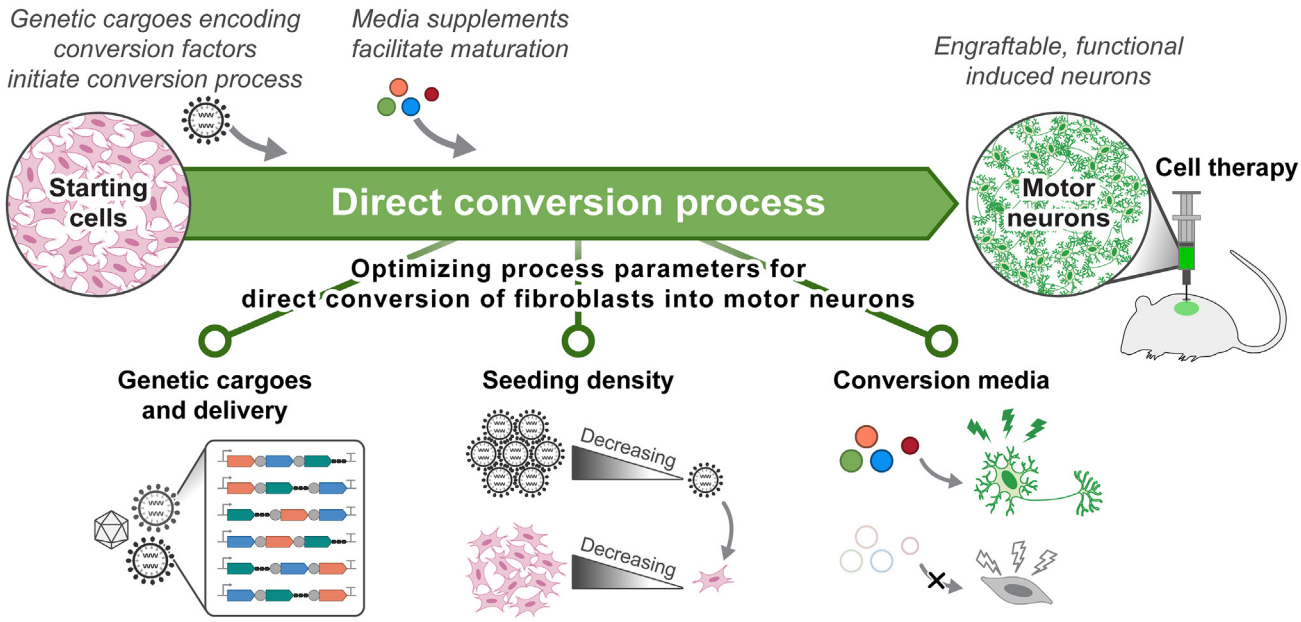

Figure 1. Robust and scalable direct conversion processes for cell therapies

Cell therapies that use converted cells will require robust and scalable cell-fate conversion processes. In our system, expression of the transcription factors via retroviruses initiates the conversion process while media supplements facilitate adoption of the new motor neuron identity. In this work, we explored how compact, genetic cargo designs encoding the conversion cocktail facilitate transfer to different viral-mediated expression systems. We also looked at how the initial seeding density of the starting cells affects conversion rates and enables low-input, high-yield direct conversion to motor neurons. Finally, we explored how robust our motor neuron conversion cocktail is to the presence of conversion media supplements.

NIL conversion module, we observed similar conversion purities across all designs. However, the yield doubles for the RIDD construct where HRAS^{G12V} is placed upstream, compared with the DDIR construct where p53DD is upstream (Figures 2E and 2F). The single cassette RIDD converts at similar yields to the original two-virus version (p53DD + HRAS^{G12V}).

Previously, we showed that cells with a history of rapid proliferation at 4 days post infection (dpi), an early time point in iMN direct conversion, convert at higher rates to more mature morphologies.[46] Thus, we hypothesized that the differences in conversion between the DDRR module designs may come from differences in proliferation rates. We identify cells that undergo a period of hyperproliferation by assaying dilution of CellTrace dye for 72 h from 1 to 4 dpi.[46] We denote cells with a history of rapid proliferation at 4 dpi as hyperproliferative (hyperP) and all other cells at 4 dpi as non-hyperP. We quantify hyperproliferation by both the percent of cells in the population that are hyperproliferative and the total number of hyperproliferative cells. As expected, the percent and number of hyperproliferative cells correlate with the percent of Hb9::GFP-positive cells at 4 dpi and the number of Hb9::GFP-positive cells at 14 dpi, respectively (Figures 2E, S1A, and S1B). However, the purity of Hb9::GFP-positive cells at 14 dpi remains unchanged across DDRR variants (Figures 2F and S1B). Putatively, the encoding of p53DD and HRAS^{G12V} generates different conversion rates due to their effects on proliferation. We confirmed that the optimal polycistronic RIDD transcript expresses p53DD and HRAS^{G12V} by a western blot (Figure S1C); however, we observed weak expression of p53DD expression from DDIR, suggesting low expression of p53DD limits conversion with DDIR.

With our optimal, single-cargo DDRR design (RIDD), we set out to optimize the motor neuron conversion module. In order to detect levels of each transcription factor, we tagged Ngn2 (Figures S1D–S1F). Through screening a variety of C-terminal tags, we identified a tagged Ngn2 variant that does not reduce conversion and allows us to identify exogenous Ngn2 by immunostaining (Figures S1G and S1H). We tested our original NIL cassette with both the untagged Ngn2 and tagged Ngn2^{x3HA}. Surprisingly, replacement of Ngn2 with Ngn2^{x3HA} in the NIL cassette increases conversion yield and purity (Figures 2G and S1J). With all three transcription factors detectable by immunofluorescence (Ngn2^{x3HA}, Isl1, and Lhx3) (Figure S1I), we next built all six permutations of the three factors in polycistronic cassettes using Ngn2^{x3HA}, Isl1, and Lhx3 separated by 2A peptides (Figures 2H and S1K). As a 3.2-kb cargo, these cassettes can be efficiently delivered by a single retrovirus to induce conversion. We did not explore IRES sequences to separate transgenes in the conversion module because their large size is less compatible with the packaging limits of therapeutically relevant vectors. Thus, we explored all six permutations of these three factors separated by an upstream P2A and downstream T2A sequence, which are reported to be the most efficiently cleaved 2A peptides.[55,56]

Addition of DDRR resulted in different trends in conversion outcomes across the cassettes. In the absence of DDRR, placement of the pioneer transcription factor Ngn2^{x3HA} upstream generates the highest yield and purity (i.e., Ngn2^{x3HA}-P2A-Isl1-T2A-Lhx3 [NIL] and Ngn2^{x3HA}-P2A-Lhx3-T2A-Isl1 [NLI]). However, with DDRR, LNI (Lhx3-P2A-Ngn2^{x3HA}-T2A-Isl1) converts at the highest rate to achieve 50% purity and 360% yield

Please cite this article in press as: Wang et al., Compact transcription factor cassettes generate functional, engraftable motor neurons by direct conversion, Cell Systems (2025), https://doi.org/10.1016/j.cels.2025.101206

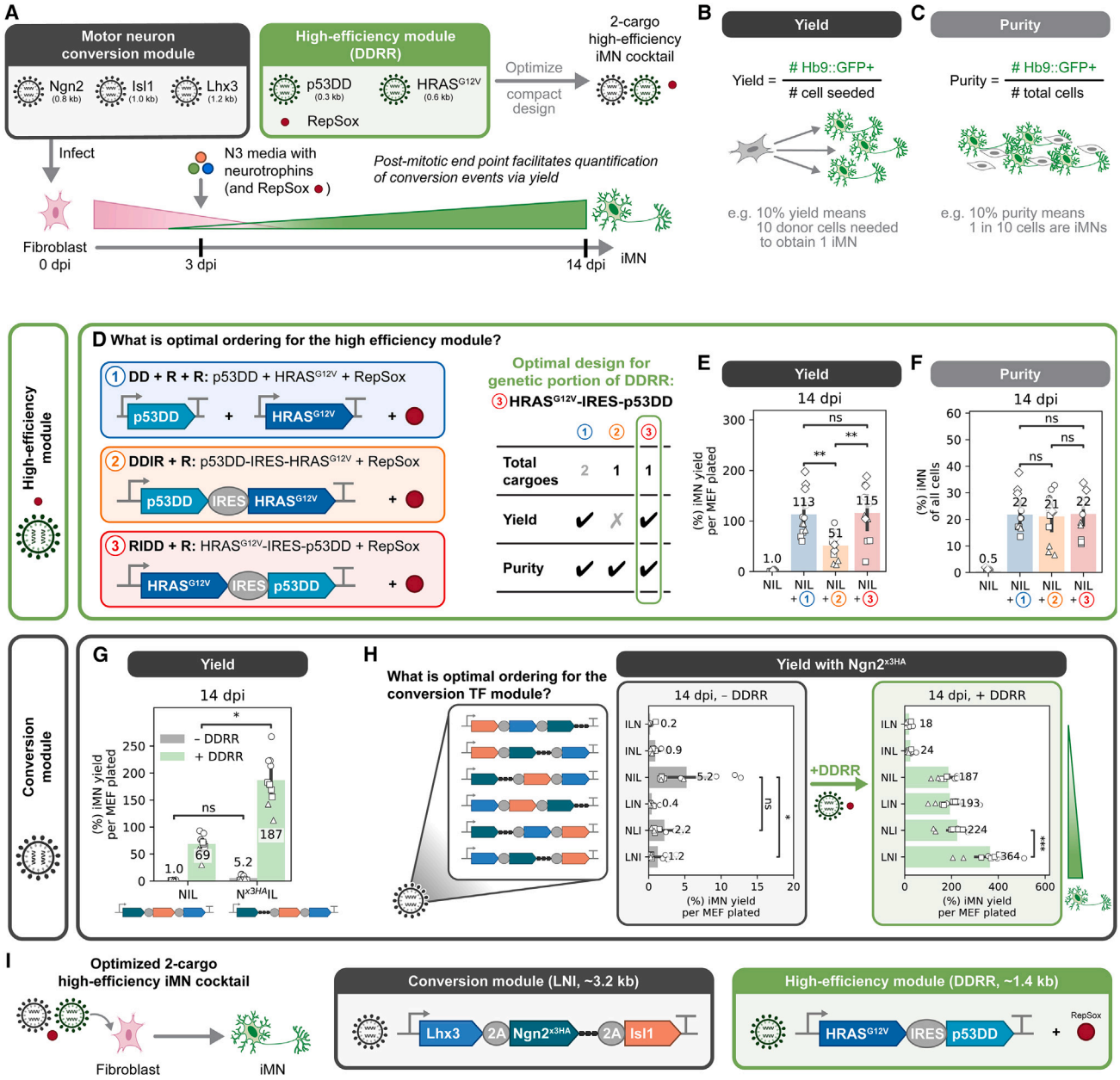

Figure 2. Optimized, compact, single-transcript cassettes increase conversion

(A) We previously identified a minimal conversion transcription factor genetic module (NIL: Ngn2, Isl1, and Lhx3) that converts fibroblasts into motor neurons at high rates with our high-efficiency chemogenetic module (DDRR: p53DD [DD], HRAS^{G12V} [R], RepSox [R]).

(B and C) Conversion rates are quantified using 2 metrics: (B) yield and (C) purity. A fluorescent Hb9::GFP reporter is used to quantify conversion rapidly in a scalable manner via flow cytometry.[51]

(D–F) (D) Different designs of the genetic portion of the DDRR cocktail lead to different (E) conversion yields and (F) purities at 14 dpi. Design 1 (DD + R): p53DD and HRAS^{G12V} on separate cassettes, design 2 (DDIR + R):p53DD-IRES-HRAS^{G12V}, and design 3 (RIDD): HRAS^{G12V}-IRES-p53DD. Mean is shown with a 95% confidence interval, and marker styles denote bio replicates. n = 4 biological replicates per condition; two-tailed t test with Bonferroni correction.

(G and H) (G) Conversion yield at 14 dpi for just the polycistronic NIL cassette ± DDRR to compare untagged Ngn2 and tagged Ngn2^{x3HA}. (H) Conversion yield at 14 dpi for the different polycistronic transcription factor cassettes without DDRR (left) vs. with +DDRR (right) in order of increasing conversion events with DDRR. All cassettes contain the tagged Ngn2^{x3HA}. Mean is shown with a 95% confidence interval, and markers denote biological replicates; n = 3 biological replicates per condition; one-tailed t test with Bonferroni correction.

(I) The optimal genetic designs screened. (1) Conversion module (LNI): Lhx3-2A-Ngn2^{x3HA}-2A-Isl1, ~3.2 kb total. (2) High-efficiency module (DDRR): HRAS^{G12V}-IRES-p53DD + RepSox, ~1.4 kb total + chemical component. Significance summary: $p > 0.05$ (ns), $^{*}p \leq 0.05$, $^{**}p \leq 0.01$, $^{***}p \leq 0.001$, and $^{****}p \leq 0.0001$.

(Figures 2H and S1K). Previously, we observed that proliferation differences can help distinguish effects of transcription factor cocktails.[46] However, we did not observe cassette-specific differences in the percent of hyperproliferative cells (Figure S1L). Thus, differences in the conversion module designs do not alter conversion by changing the rate of proliferation.

We hypothesized that differences in the levels of transcription factors may explain differences in the conversion rates between the various encodings. We measured the levels of each transcription factor in single cells using immunofluorescence and quantified it by flow cytometry. For the detection of Ngn2^{x3HA}, we could directly measure the transgenic protein via the hemagglutinin (HA) tag. However, for Isl1 and Lhx3 staining, we measured total levels of protein, including endogenous and exogenous protein expression. We observed that each cassette design led to a range of expression levels across the bulk population (Figure S1I).

Based on our previous findings, we expected that driving proliferation with the DDRR module should decrease all three transcription factor levels by increasing the fraction of hyperP cells during conversion.[46,51] Indeed, across all conversion cassette designs, we observed that transcription factor levels are all lower in the presence of DDRR (Figures S2A and S2B). We also confirmed that transcription factor expression is lower in cells with a history of hyperproliferation (Figure S2C). To examine proliferation-mediated and cassette-specific effects on transcription factor levels in high-efficiency conversion, we looked at Ngn2^{x3HA}, Isl1, and Lhx3 levels in the hyperP and non-hyperP conversion subpopulations when DDRR is included (Figure S2D). The least effective cassettes (ILN or INL with DDRR) have low expression of all three transcription factors at the bulk population level (Figure S2A) as well as in the hyperP cells (Figure S2D) but markedly lower levels of Ngn2^{x3HA} and Isl1 than all the other designs. Interestingly, when controlling for the presence of DDRR, expression of Lhx3 was broadly reduced in hyperproliferative cells while Ngn2 and Isl1 were minimally affected (Figure S2D).

Based on our previous titration of the individual transcription factors Ngn2, Isl1, and Lhx3,[46] we expected cassettes with the highest Ngn2^{x3HA} and lowest Lhx3 levels to convert at the highest rate. However, the best-performing design, LNI, does not have the highest Ngn2 nor the lowest Lhx3 levels (Figure S2A). Potentially, the relative ordering of factors may influence their rates of cleavage around the P2A and T2A elements, which may or may not influence their activity.[61] Notably, detected differences in transcription factor expression are relatively small (Figure S2A). Together, these results demonstrate that the encoding of transcription factors in polycistronic cassettes influences the expression of the factors, and this influence is independent of differences in proliferation history. For small design spaces, functional screening of single-transcript cassettes of conversion factors remains the best approach for optimization (Figure 2I).

Compact, single-transcript cassettes are portable to lenti and AAV for comparison of conversion

Viruses provide an efficient delivery method to achieve sustained transgene expression for conversion. Different viruses offer different safety profiles, cargo limits, and levels and duration of expression (Figure 3A). However, viral packaging limits set constraints on the size of cargoes, limiting design and mechanisms of regulation. Designing compact conversion cargoes improves the flexibility of design choice for viral expression. In a well-controlled *in vitro* setting of conversion, we sought to explore these trade-offs using our compact design, which can port between retrovirus, lentivirus, and AAV. *In vitro*, we can parse limits of our conversion cocktails that may be inherent to the level of expression from the vector. Understanding how viral systems compare independent of *in vivo* delivery limitations can guide designs for performance *in vivo*.

We first explored delivery of the conversion cocktail via single-stranded AAVs. AAVs are FDA-approved for a range of clinical applications to deliver transgenes *in vivo* for vaccines and gene therapies.[62] AAVs are preferred for *in vivo* applications as they have low immunogenicity and cytotoxicity profiles and do not usually integrate into target cells' genomes. However, a main limitation of AAVs is that they can only package up to ~4.7 kb, including the promoter, transgene of interest, and polyadenylation sequence. To determine transduction efficiency, we used a control AAV-CAG-GFP to titrate AAV dosing for MEF transduction with a range of 10^6 to 10^2 genome copies (GCs) per cell (Figure S3A). We used serotyped AAV2, as they have been reported to be the best at transducing human and mouse fibroblasts.[63–67] We compared AAV-CAG-GFP expression with expression of a retroviral pMXs-GFP vector at 4 dpi. Retroviruses efficiently transduce MEFs, with >90% of cells having detectable GFP expression at 4 dpi (Figure S3A). By contrast, AAVs infect MEFs poorly with a maximum transduction efficiency of 37% at a high dosing of 10^6 GC per cell. Further, in transduced cells with detectable GFP, constitutive retroviral expression is roughly one order of magnitude higher than that of strong AAV-CAG-GFP expression (Figure S3B). Our maximum transduction efficiency matches the range of those found in literature.[63–67] Thus, poor AAV transduction efficiency results in much lower transgene expression levels compared with retroviruses in MEFs. Putatively, lower AAV expression is due to lower copy number of infection rather than inherent expression differences between AAV-CAG and retroviral pMXs (e.g., promoter strength).

Though AAV transduction efficiency of MEFs is limiting, we tested the AAV vectors for expression of conversion factors and conversion (Figure 3B). Low transduction rates might prevent efficient co-delivery of both the conversion and high-efficiency modules. However, we reasoned that the likelihood a given initial MEF would receive both modules was still higher for two genetic cargoes (LNI + DDR) rather than the initial five (Lhx3 + Ngn2 + Isl1 + p53DD + HRAS^{G12V}). To support high expression, we used the strong CAG promoter to drive expression of the DDR transgenes for the high-efficiency module (DDR; p53DD, HRAS^{G12V}; ~1.4 kb) and the medium-strength but more compact CMV promoter[68] to drive expression of the larger conversion module (LNI; Lhx3-2A-Ngn2^{x3HA}-2A-Isl1; ~3.2 kb) (Figure 3B). We also added the fluorescent SNAP-tag onto p53DD to detect DDR expression and screened for a single-transcript design that optimized conversion for retroviral delivery (Figure S3C). We used SNAPp53DD-IRES-HRAS^{G12V} as the optimal SNAP-tagged DDR cassette, as it results in a higher yield with similar purity as HRAS^{G12V}-IRES-SNAPp53DD, contrary to what was seen with the untagged p53DD variant (Figures 2D–2F).

Please cite this article in press as: Wang et al., Compact transcription factor cassettes generate functional, engraftable motor neurons by direct conversion, Cell Systems (2025), https://doi.org/10.1016/j.cels.2025.101206

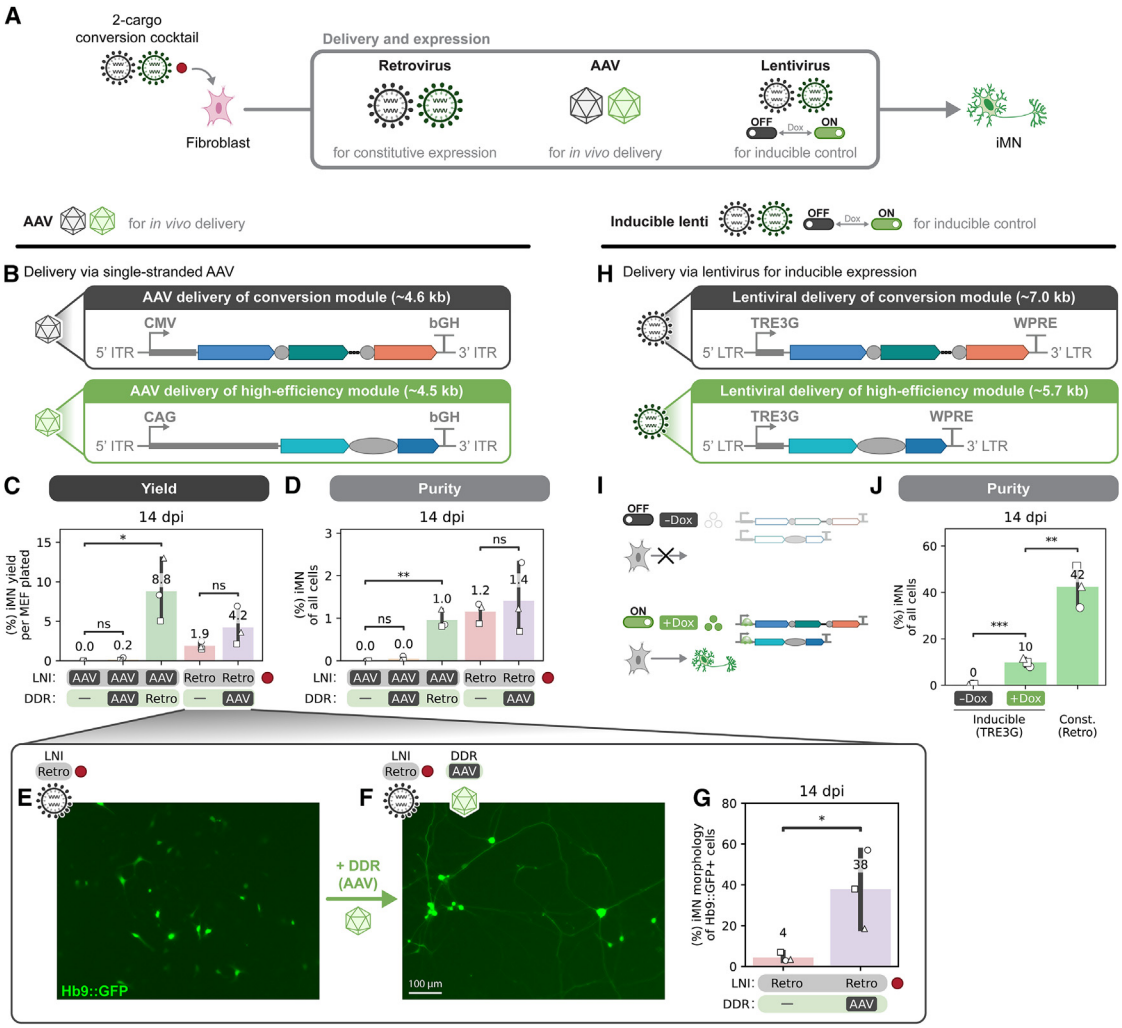

Figure 3. Compact, single-transcript cassettes are portable to lenti and AAV for comparison of conversion

(A) Compact conversion cassettes can be ported into different delivery and expression modalities. Traditional retroviruses are constitutively expressed. We explored AAV for future *in vivo* work and lentiviruses to enable inducible, transcriptional control.

(B–D) Conversion using single-stranded AAVs (AAV). (B) The design of the conversion (LNI) and high-efficiency (DDR; SNAPp53DD-IRES-HRAS^{G12V}) modules for AAV expression. The conversion yield (C) and purity (D) at 14 dpi using AAVs or retroviruses to drive expression of either the conversion (LNI) or high-efficiency (DDR) modules. All conditions were converted with RepSox. Mean is shown with a 95% confidence interval, and markers denote biological replicates; $n = 3$ biological replicates per condition; two-tailed t test.

(E–G) Morphological differences between Hb9::GFP cells when converted from retrovirus-LNI ± AAV-DDR. Representative images of Hb9::GFP for retrovirus-LNI (E) and retrovirus-LNI + AAV-DDR (F). Both conditions were converted with RepSox. (G) The percent of Hb9::GFP-positive cells with a neuronal morphology (tight soma with neurites) was quantified from all Hb9::GFP-positive cells detectable for $n = 3$ biological replicates per condition and one-tailed t test. Scale bar represents 100 µm.

(H–J) Conversion using lentiviruses for inducible expression. (H) The design of the conversion (TRE3G-LNI) and high-efficiency (TRE3G-DDR; SNAPp53DD-IRES-HRAS^{G12V}) modules for inducible expression. (I) Schematic for inducible expression where addition of dox turns on expression of both modules. rtTA was expressed using a retrovirus for all conditions so TRE3G transcription would activate in the presence of dox. The conversion purity (J) at 14 dpi using inducible lentiviruses (TRE3G-LNI + TRE3G-DDR + retro-rtTA) with and without dox, and in comparison with constitutively (const.) expressed retroviruses (retro-LNI + retro-DDR; SNAPp53DD-IRES-HRAS^{G12V}). All conditions were converted with RepSox. Mean is shown with a 95% confidence interval, and markers denote biological replicates; $n = 3$ biological replicates per condition; two-tailed t test. Significance summary: $p > 0.05$ (ns), $^{*}p \leq 0.05$, $^{**}p \leq 0.01$, $^{***}p \leq 0.001$, and $^{****}p \leq 0.0001$.

For all AAV experiments, we included the chemical supplement, RepSox (R), and using our titration results, transduced cells with an equivalent GC dose to achieve a multiplicity of infection (MOI) of MOI = 5 (i.e., 1.1×10^7 GC/cell) for each virus. We first tested AAV-CMV-LNI with and without AAV-CAG-DDR. We did not observe conversion when modules were delivered by AAV alone (i.e., AAV-CMV-LNI ± AAV-CAG-DDR). However, AAV-CMV-LNI with retrovirally delivered DDR (retro-DDR) was sufficient to yield converted iMNs from MEFs (Figures 3C and 3D). Thus, AAV-mediated delivery of the conversion module LNI can induce direct conversion of MEFs into iMNs but only in the presence of stronger expression mediated by retro-DDR.

Please cite this article in press as: Wang et al., Compact transcription factor cassettes generate functional, engraftable motor neurons by direct conversion, Cell Systems (2025), https://doi.org/10.1016/j.cels.2025.101206

We reasoned that while entirely AAV-mediated expression is not currently sufficient for direct conversion of MEFs, potentially retroviral expression of the conversion module with transient AAV delivery of the high-efficiency DDRR module's oncogenes may improve the safety profile of converted cells. Thus, we compared retro-LNI expression with and without AAV-DDR. While we did not observe significant increases in conversion rates (Figures 3C and 3D), we observed that AAV-DDR improves the morphologies of Hb9::GFP-positive, retroviral LNI-converted cells at 14 dpi (Figures 3E–3G). Together, these data suggest that transient delivery of the high-efficiency DDR oncogenes during the conversion process can improve converted cells' morphologies. Currently, AAV transduction efficiency is limiting for the conversion of fibroblasts. Improved delivery vectors and different starting cell types may increase the direct conversion rates achieved with AAVs.

In addition to improving compatibility with diverse delivery vehicles, compact cassettes offer simple single-transcript control. As proof of principle, we employed the commonly used Tet-based activator system to demonstrate inducible control of the conversion (TRE3G-LNI) and high-efficiency modules (TRE3G-DDR) via lentiviruses (Figure 3H). Using retrovirally delivered reverse tetracycline-controlled transactivator (rtTA), addition of doxycycline (dox) induces transcription from the TRE3G promoter (Figure 3I). Without dox, we did not observe conversion (Figure 3J). In the presence of dox, we generate iMNs, albeit at a lower rate compared with constitutive retroviral expression (Figure 3J). The inducible system allowed us to examine the stability of cell identity in the absence of transgene induction. 2 weeks following the removal of dox, we still observe Hb9::GFP-positive iMNs (Figure S3D), demonstrating that iMNs are stable without continuous activation of the conversion cocktail. Putatively, differences in expression levels between the TRE3G-expressed transgenes in the lentivirus compared with the retroviruses lead to different conversion rates. We chose to use constitutive retroviral expression for the rest of this study due to its high transduction efficiency with MEFs and its simplicity of production and expression (i.e., no auxiliary activators needed).

Compact cassettes support scale up of the conversion process to generate large numbers of neurons

With optimized, single-transcript genetic cargoes, we next sought to improve the conversion process by adjusting the initial seeding density of the starting cells. Decreased seeding density improves conversion to iPSCs.[69] Lower initial seeding density encourages proliferation and may prevent overcrowding of the cells at later time points as they expand. Further, starting with fewer initial cells reduces the amount of input material (i.e., the number of starting cells and the amount of virus) required to achieve the same number of converted cells (Figure 4A). Reducing the seeding density may allow reductions in other reagents include the volumes of viruses required. For applications requiring high numbers of converted cells, such as cell therapy, reducing input materials is crucial for scalable manufacturing.

Exploring transcript design, we found that ordering of the transcription factors in polycistronic cassettes influences transcription factor levels and conversion rates, though correlations between the two are weak (Figures 2H and S2A). However, proliferation can change how cells respond to different transcription factor levels.[46] Thus, we hypothesized that the impact of subtle differences in the expression from individual cassettes might diminish over increasing rounds of cell division and lead to broad increases in yield. Thus, we aimed to increase proliferation and extend the number of divisions by decreasing the initial seeding density of starting cells. We selected two cassettes: a poor-performing cassette (INL) and the best-performing cassette (LNI). To confirm that expansion via proliferation was improving conversion, we also included an LNI + Brn2 control to repress proliferation during high-efficiency conversion with DDRR as Brn2 is a potent repressor of proliferation.[46] Additionally, we maintained a constant MOI by serially diluting viral supernatant to match the dilution of the initial density of seeded cells from 10,000 to 1,250 per 96-well (8-fold dilution) (Figure 4B). For this set of experiments, we used spinfection, a process of centrifuging cells following addition of viral supernatant, to enhance transduction efficiency at low seeding densities. We quantified conversion by 3 metrics at 14 dpi: total yield, normalized yield, and purity. We typically quantify yield and purity; however, here we make a distinction between two types of yield: "total yield" and "normalized yield." Total yield is the total number of iMNs detected per well. Normalized yield is the typical yield we quantify, representing the total yield (or total number) of iMNs divided by the initial number of starting cells.

By decreasing seeding density at constant MOI, we found that the total yield of converted iMNs increased slightly but remained relatively constant while normalized yield and purity increased across both LNI and INL cassettes (Figures 4C–4E). Because similar total yields of iMNs are obtained with 8-fold fewer initial cells, we observe extremely high normalized yields of greater than 1,000%, meaning more than 10 iMNs obtained per MEF plated. Remarkably, low seeding densities yield purer end populations with neuronal morphologies at 14 dpi (Figure S4A). Notably, while conversion with INL is lower than LNI by all metrics at the typical seeding density of 10,000 per 96-well, these differences are diminished at lower initial seeding densities. Further, inclusion of Brn2 with LNI eliminates any gain in conversion with reduced seeding density (Figures 4C–4E). To look at cell expansion over time, we used flow cytometry to assay wells at various time points for a given conversion replicate. By tracking cell counts normalized to the initial seeding density over time, we confirm that decreasing initial seeding density increases proliferation early in conversion across all cassettes except when Brn2 is included (Figure 4F). At higher seeding densities, expansion of the cell count plateaus in the middle of conversion, putatively, due to overcrowding of cells in a well. We observe a small reduction in the cell count near the later stages of conversion at the lowest seeding density of 1,250 per 96-well, which we attribute to increasing fragility of cells during media changes for sparser and more neuronal populations. As conversion continues, we see increasingly pure Hb9::GFP-positive cultures as a greater fraction of cells activate the Hb9::GFP reporter (Figure S4B). Thus, by decreasing seeding density, we obtain a larger number and fraction of converted Hb9::GFP-positive cells. We conclude that the optimal process uses a seeding density of 2.5k MEFs per 96-well with the compact LNI + DDRR modules.

Please cite this article in press as: Wang et al., Compact transcription factor cassettes generate functional, engraftable motor neurons by direct conversion, Cell Systems (2025), https://doi.org/10.1016/j.cels.2025.101206

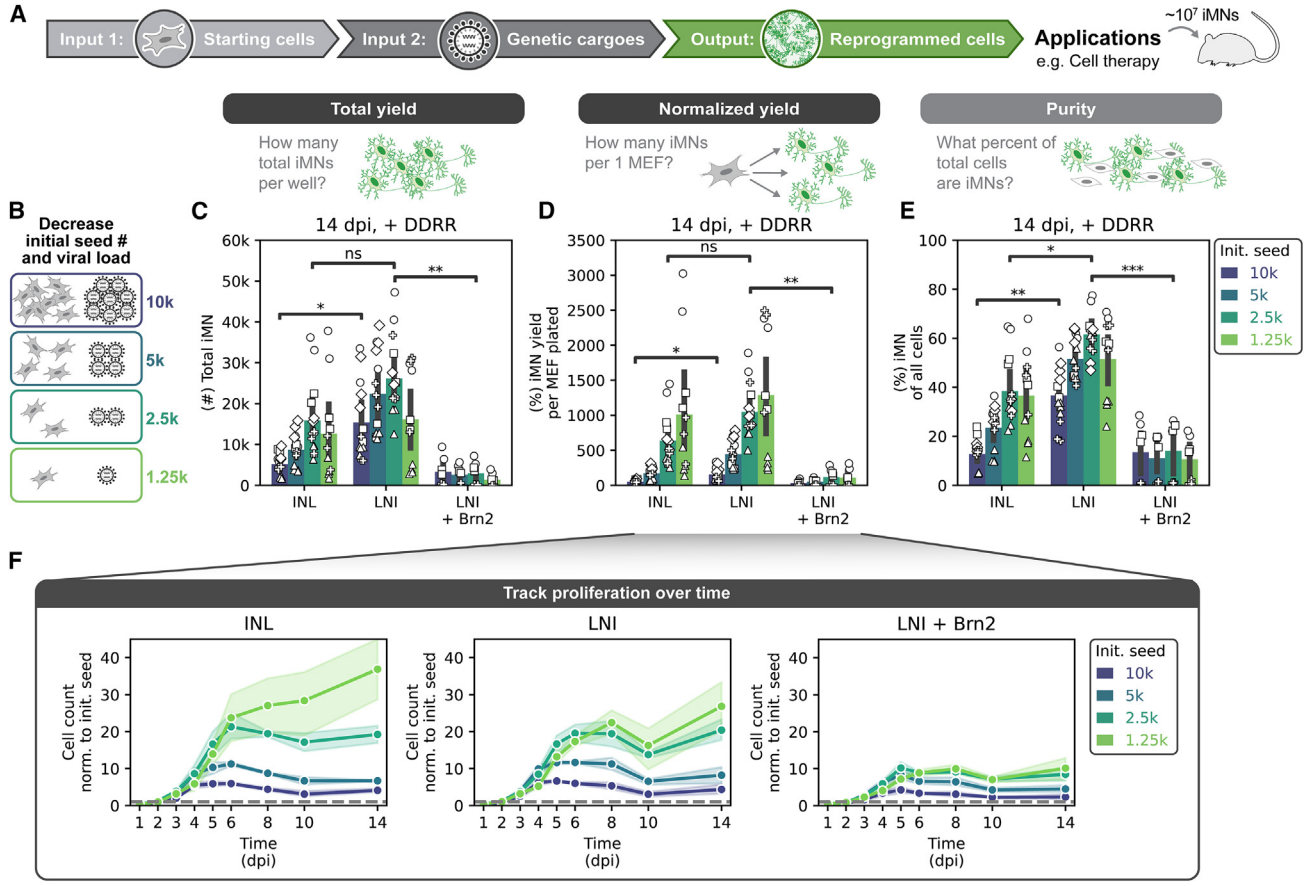

Figure 4. Compact cassettes support scale up of the conversion process to generate large numbers of neurons

(A) Downstream applications for converted cells require efficient conversion processes (e.g., cell therapies that require ~10^7 cells/treatment) that ideally require low-input material amounts. Limiting factors for direct conversion are usually the number of starting cells and the successful delivery of genetic cargoes required to drive the conversion process.

(B–E) Conversion using decreasing amounts of starting cells and virus. MEFs were seeded at different seeding densities per 96-well and spinfected with similarly decreasing amounts of viral supernatant (B). Cells and conversion TF cocktails were serially diluted in the same ratio of 1:2. All conditions were converted +DDRR. Conversion at 14 dpi was quantified by (C) total yield (the total number of iMNs cells detected), by (D) normalized yield (the total number of iMNs divided by how many cells were initially seeded), and by (E) purity (the percent of cells detected that are iMNs). Mean is shown with a 95% confidence interval, and markers denote biological replicates; n = 3–5 biological replicates per condition; two-tailed t test.

(F) Cell count as detected by flow from 1 to 14 dpi, normalized to the number of initially seeded cells. Mean is shown with a 95% confidence interval; n = 2 biological replicates per condition. Significance summary: $p > 0.05$ (ns), $^{*}p \leq 0.05$, $^{**}p \leq 0.01$, $^{***}p \leq 0.001$, and $^{****}p \leq 0.0001$.

Given that $Ngn2^{x3HA}$ levels correlate well with conversion, we measured $Ngn2^{x3HA}$ across seeding densities early in conversion at 4 dpi. Increasing the proliferation rate by changing the initial seeding density did not change $Ngn2^{x3HA}$ levels substantially (Figure S4C). As seen previously, transcription factor levels are set by the cassette design (Figure S2A). Thus, increasing proliferation rate can improve conversion rates across transcription factor encodings independent of transcription factor levels. Interestingly, adding Brn2 to LNI-induced conversion increases $Ngn2^{x3HA}$ levels slightly. Putatively, lower rates of proliferation lead to higher transcription factor levels.[46] Together, these data show that decreasing seeding density supports scaling production of converted cells as it reduces the input of both cells and virus while improving conversion rates in terms of both normalized yield and purity. Increasing direct conversion rates with low amounts of input materials will help realize the potential of conversion for downstream applications, such as cell therapies that require large numbers of cells.

Compact cocktail produces electrically active induced neurons at scale

During *in vitro* direct conversion, transcription factors direct cell fate in combination with external signaling cues from growth factors and other biochemicals. Conversion protocols often rely on specific cocktails of small molecules and growth factors.[51,70] Robust conversion processes should ideally be minimally perturbed by variations (e.g., timing and concentration) in media supplements. Typically, our conversion protocol switches to N3 media with media supplements at 3 dpi onward to facilitate maturation. We wondered how media perturbations might impact the conversion process. To explore how robust our conversion cocktail is to perturbations in media, we converted cells with and without neurotrophic growth factors (brain-derived

Please cite this article in press as: Wang et al., Compact transcription factor cassettes generate functional, engraftable motor neurons by direct conversion, Cell Systems (2025), https://doi.org/10.1016/j.cels.2025.101206

CellPress

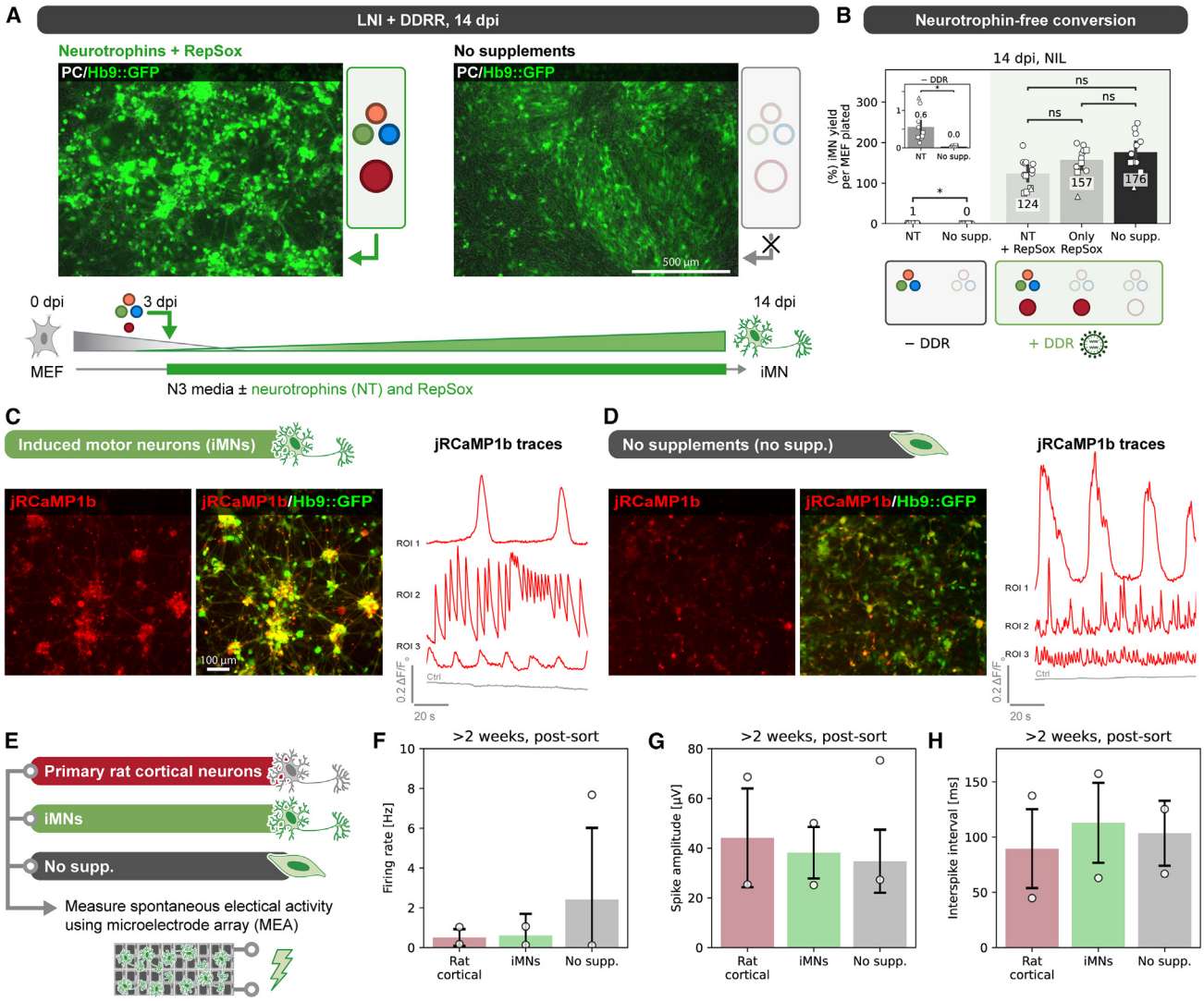

Figure 5. Compact cocktail produces electrically active induced neurons at scale

(A) Images of cells at 14 dpi converted by LNI + DDRR, in N3 media containing neurotrophins (NTs) and RepSox (left) or with no supplements (right), starting from 3 dpi. Scale bar represents 500 µm.

(B) Conversion yield at 14 dpi for NIL ± DDRR. NIL-infected cells were converted in N3 media ± NTs. NIL + DDRR-infected cells were converted in N3 media starting at 3 dpi with both NT and RepSox, with only RepSox, or with neither. Inset shows iMN yield for NIL (without DDRR) with zoomed-in axis for clarity. Mean is shown with a 95% confidence interval, and markers denote biological replicates; n = 3 biological replicates per condition; two-tailed t test with Bonferroni correction.

(C and D) Spontaneous Ca^{2+} imaging using the fluorescent jRCaMP1b reporter in converted Hb9::GFP-positive cells sorted at 14 dpi and allowed to recover for 7 days. Representative images of Hb9::GFP-positive cells converted with NTs + RepSox (C, left) or without any supplements (D, left). Scale bar represents 100 µm. Representative traces of normalized jRCaMP1b fluorescence ($\Delta F/F_o$) over time for three manually selected regions of interest (ROIs) for both conditions (C and D, right). A control ROI containing no spontaneous spiking is shown for each. $\Delta F/F_o$ was calculated as $(F-F_o)/F_o$ where F is the fluorescence over time and F_o is the minimum fluorescence detected for that ROI.

(E–H) Spontaneous electrical activity detected by a multielectrode array (MEA). Measurements were taken ~18 h after media change with BrainPhys. Converted Hb9::GFP-positive cells cultured with NTs + RepSox (green, middle) or without any supplements (gray, right) were sorted at 14 dpi and allowed to recover for >2 weeks with or without NT + RepSox, respectively. Primary rat cortical neurons (left, red) recovered for >2 weeks in N3 media with NT + RepSox were included as a positive control. (F–H) Spontaneous electrical activity was quantified by (F) firing rate, (G) spike amplitude, and (H) interspike interval. Mean is shown ± standard deviation, and range is shown with markers for the 10th and 90th percentiles. n = 1 biological replicate per condition. See Figures S5B–S5D for histograms. Significance summary: $p > 0.05$ (ns) and $^*p \leq 0.05$.

neurotrophic factor [BDNF], ciliary neurotophic factor [CNTF], glial cell line-derived neurotrophic factor [GDNF], and fibroblast growth factor [FGF]) and the small-molecule TGF-β-inhibitor, RepSox, in our high-efficiency DDRR module. In the absence of neurotrophins and RepSox, our compact LNI + DDR transgenic modules still generate Hb9::GFP-positive cells at high rates (Figures 5A, 5B, and S5A). However, without both neurotrophins and RepSox, Hb9::GFP-positive cells adopt more

Please cite this article in press as: Wang et al., Compact transcription factor cassettes generate functional, engraftable motor neurons by direct conversion, Cell Systems (2025), https://doi.org/10.1016/j.cels.2025.101206

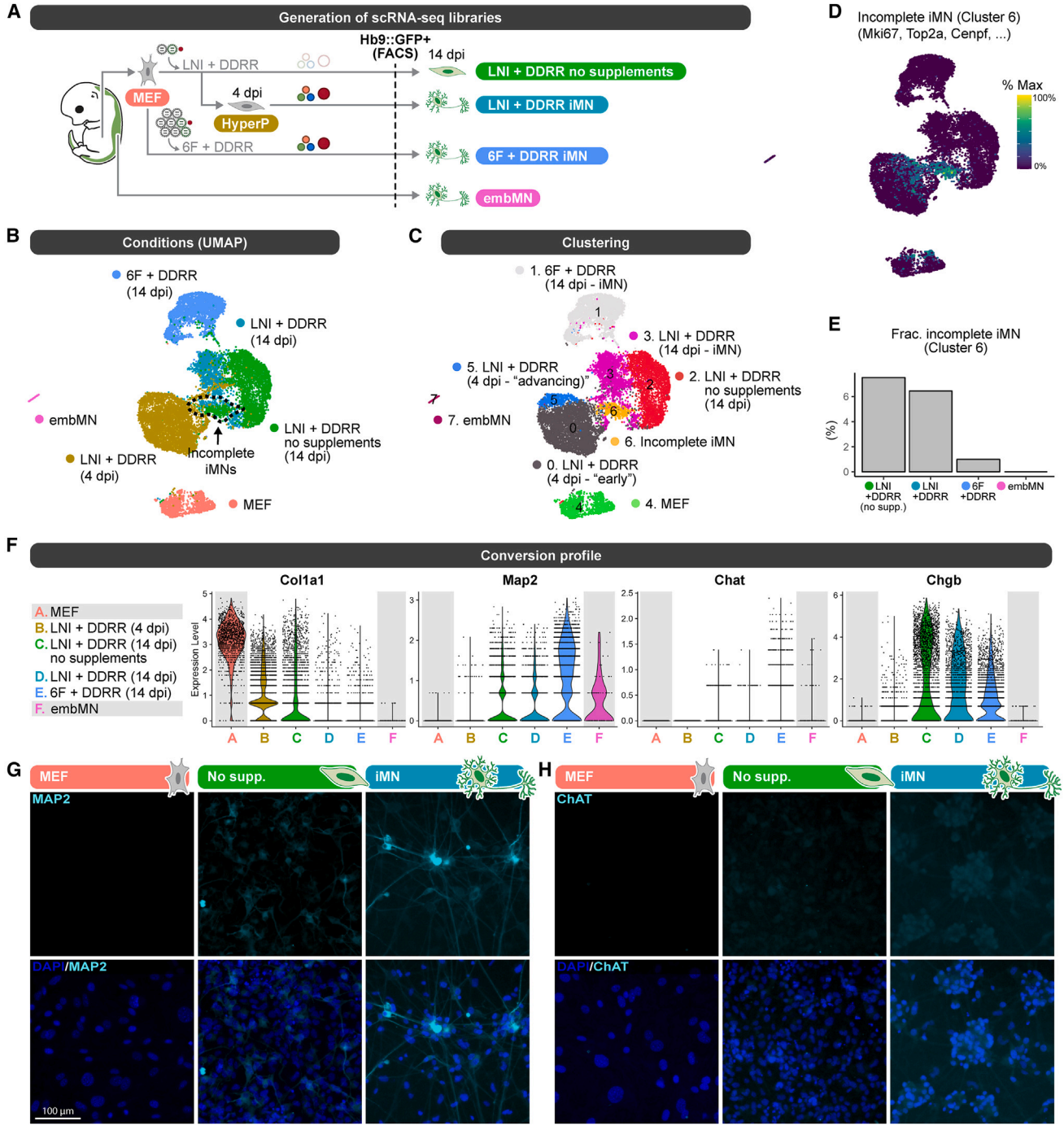

Figure 6. Conversion cocktail and conditions influence the cell states of induced motor neurons

(A) Schematic of which conditions were used to generate scRNA-seq libraries to assess transcriptional states in highly efficient conversion. Embryonic motor neurons (embMNs) and mouse embryonic fibroblasts (MEFs) serve as end and initial cell identity references. LNI is the polycistronic cassette with Ngn2^{x3HA}. embMNs were isolated from a primary Hb9::GFP-positive spinal cord at E13.5. Both embMN and all 14 dpi conditions were sorted for Hb9::GFP-positive cells prior to loading for scRNA-seq, and LNI + DDRR 4 dpi was sorted for hyperP cells only. LNI + DDRR 14 dpi iMNs were converted either with or without NT and RepSox starting at 3 dpi (see Figure 3A).

(B) UMAP of different conversion conditions. embMNs were bioinformatically isolated based on Isl1, Lhx3, and Hb9 (Mnx1) expression ($n = 91$). The LNI + DDRR 4 dpi only contains hyperP cells, and all 14 dpi iMNs only contain sorted Hb9::GFP-positive cells.

(C) Clustering of UMAP from Figure 4B. Annotated clusters were determined by looking at overlap with conversion conditions (Figures 4B, 4C, and S5A) and by looking at cluster biomarkers.

(D) Incomplete converted motor neurons revealed by clustering. Mki67 expression is shown, but other genes expressed during G2/M (e.g., Top2a and Cenpf) show similar trends.

(legend continued on next page)

fibroblast-like morphologies (Figure 5A). Without expression of the DDR transgene, Ngn2, Isl1, and Lhx3-induced direct conversion cannot generate Hb9::GFP-positive cells without neurotrophins (Figures 5B and S5A). Together, these data suggest the high-efficiency, genetic DDR module makes our direct conversion process more robust to perturbations in the conversion media. However, neurotrophic factors and RepSox supplements support neuronal maturation via morphological remodeling.

In vitro-derived cells display a spectrum of functional maturity.[4,71] Previously, we observed that our high-efficiency module improves the morphological, transcriptional, and electrophysiological profile of iMNs.[51] Given that media supplements are dispensable for Hb9::GFP activation with the DDR module but affect morphologies, we wondered how functional properties such as calcium signaling and electrical activity would compare to those for primary neurons and cells converted in different media conditions. We converted MEFs with the LNI + DDR transgenic modules and a retroviral-delivered, fluorescent, genetically encoded Ca^{2+} indicator, jRCaMP1b.[72] We used fluorescence-activated cell sorting (FACS) at 14 dpi to isolate Hb9::GFP-positive cells converted with or without media supplements, which we term iMNs or non-supplemented (no supp.), respectively. After a 1-week recovery period, we confirmed both iMNs and non-supplemented cells show a range of spontaneous Ca^{2+} signaling (Figures 5C and 5D and Videos S1 and S2).

Next, we plated Hb9::GFP-positive cells onto a high-density multielectrode assay (MEA) to directly measure electrical activity (Figure 5E). Following plating onto the MEA, we encountered challenges in neuron adherence, as observed by others, in the long-term culture of neurons.[73] We chose to use primary rat cortical neurons as a positive control for primary neurons. Primary rat cortical neurons reflect mature, accessible *in vivo*-derived neurons. For successfully adhered cells, iMNs generated with media supplements achieved a smaller range of firing rates that more closely matched the primary rat cortical neurons compared with cells derived without media supplements, as expected (Figures 5F and S5B–S5D). However, Hb9::GFP-positive cells converted with or without media supplements still show spontaneous spike amplitudes and interspike intervals comparable to primary rat cortical neurons (Figures 5G, 5H, and S5B–S5D).

Collectively, our data demonstrate that our compact LNI + DDRR cocktail can convert cells into functional motor neurons. Media conditions can be most easily controlled *in vitro* during conversion. While media supplements support the most robust maturation, we observe features of functionality even in the absence of media supplements, indicating a robust process for establishing neuron-like cells and supporting the potential for deriving functional cells in environments with minimal neurotrophic support, such as those *in vivo*. Future work can explore the specific effects and temporal requirements of neurotrophins and RepSox on generating functionally mature iMNs via direct conversion.

Conversion cocktail and conditions influence the cell states of iMNs

In the absence of media supplements, cells converted with the compact LNI + DDR transgenic modules can activate the Hb9::GFP reporter and demonstrate spontaneous electrical activity. Thus, we wondered in what ways beyond morphology these non-supplemented Hb9::GFP-positive cells differed from iMNs generated with media supplements. To examine the transcriptional states of our converted cells, we generated and sequenced single-cell RNA sequencing libraries of cells collected across the conversion timeline and in the absence of media supplements (Figure 6A). We induced conversion using the compact LNI + DDRR cocktail and collected Hb9::GFP-positive cells by FACS at 14 dpi. With this cocktail, we collected cells converted either with or without media supplements. We also collected hyperproliferative cells at 4 dpi to capture early transcriptional states in the conversion process. We used MEFs and embryonic motor neurons (embMNs) as reference cell states for the beginning and target cell types.

In the hyperproliferative cells early on at 4 dpi, we identified a cluster with increased expression of transcription factors involved in neurogenesis but not included in the conversion module, including Bhlhe22 and Neurod1,[74] suggesting these cells may be advancing toward iMNs (Figures 6B, 6C, and S6A). Further, conversion module transcription factors also express at higher levels in the "advancing" state. These data are consistent with a model in which high expression of the transcription factors drives hyperproliferative cells, which are more receptive to conversion, to convert at high rates.[46] Considering Hb9::GFP-positive cells at 14 dpi, we were able to identify a cluster (cluster 6) of incompletely converted cells present across conversion cocktails and media conditions (Figures 6D and 6E). Although Hb9::GFP-positive, these cells are enriched for markers of proliferation (e.g., Mki67) and appear as a small fraction of cells across cocktails (<7%, Figures 6E and S6B). The higher percent of incomplete iMNs in LNI + DDRR compared with 6F + DDRR is consistent with our observation that the three-transcription factor cocktail expands the population and window of time over which cells proliferate and convert.[46]

To compare different cocktails, we focused on the fully converted populations of motor neurons by excluding cluster 6. Across the different conversion cocktails, we observe differences in markers of maturity (Figure 6F). Differences in markers of neuronal maturity between iMNs and embMNs may be attributed to the early developmental stage from which the primary embMNs were isolated (embryonic day [E]13.5). As expected from the

(E) Percentage of cells in the incomplete iMN cluster 6 across conversion conditions at 14 dpi with embMN as a baseline.
(F) Violin plots of scRNA expression of stereotypical markers of MEFs (Col1a1) and motor neuron maturation (MAP2, ChAt, Chgb) for conversion conditions after incomplete iMN cluster 6 is removed for representative genes of motor neuron identity.
(G and H) (G) Immunofluorescence for stereotypical markers of motor neuron maturation (MAP2, ChAT) for MEFs (left), Hb9::GFP-positive cells converted without any supplements (No supp., middle) and iMNs converted with NTs + RepSox (iMN, right). Staining for MAP2 (H) is shown without (top) and with DAPI (bottom). Staining for ChAT (I) is shown without (top) and with DAPI (bottom). Converted iMNs were sorted for Hb9::GFP-positive cells at 14 dpi and allowed to recover to 7 weeks with or without NTs + RepSox for iMNs and iMNs (no supp.) conditions, respectively. Control MEFs were also sorted for viability at the same time and allowed to recover 7 days.

Please cite this article in press as: Wang et al., Compact transcription factor cassettes generate functional, engraftable motor neurons by direct conversion, Cell Systems (2025), https://doi.org/10.1016/j.cels.2025.101206

observed morphologies (Figure 5A), excluding media supplements in LNI + DDRR generates cells with elevated expression of the fibroblast-specific matrix protein Col1a1. Expression of the transcription factors, Ngn2 and Lhx3, does not significantly differ between the converted iMNs and embMN, whereas Isl1 expression is lower in iMNs compared with embMNs (Figure S6C). Given that we see different transcriptional profiles between LNI + DDRR converted cells with and without supplements, we stained for neuronal markers microtubule-associated protein 2 (MAP2) and cholinergic marker choline acetyltransferase (ChAT). ChAT produces the neurotransmitter acetylcholine that motor neurons use to control motor behavior. We confirm differences in Hb9::GFP-positive cells as conversion with supplements generate iMNs with higher MAP2 and ChAT (Figure 6G). Together, these observations demonstrate that cells activating the Hb9::GFP reporter are electrically active and display the expected expression of enzymes specific to motor neurons but occupy distinct states influenced by their conversion cocktail and media conditions.

A compact cocktail generates engraftable neurons by direct conversion

Using cellular conversion to generate autologous cell grafts from accessible cell donor populations holds great potential for the personalized replacement of damaged or diseased tissues and organs. However, realizing the potential of reprogrammed cell therapies requires the development of efficient and scalable manufacturing processes, and low rates of direct conversion have up until now limited the use of this approach in CNS applications. Additionally, while grafted cells may promote therapeutic effects, these outcomes may be diminished by poor transplanted cell survival.[75] In generating large numbers of functional, iMNs at scales relevant for neural cell-based therapies (e.g., millions of cells[76]; Figure S7A), we next wanted to test whether allogeneic Hb9::GFP-positive cells converted with our cocktail could survive and integrate when transplanted into the mouse CNS. Following LNI + DDRR conversion, we FACS-isolated and then transplanted Hb9::GFP-positive cells into healthy C57BL/6 mouse brains as well as in mice that had been subjected to a small acute N5-(1-Iminoethyl)-L-ornithine (L-NIO) induced stroke-injury 2 days prior (Figure 7A). Grafted cells could be readily detected in brain sections by antibody detection of HA due to constitutive $Ngn2^{x3HA}$ expression from the conversion module, as well as by GFP fluorescence. The striatum was chosen for initial proof of principle for iMN grafting because it is a readily accessible anatomic site that allows for reproducible injuries and transplantation injections in a neural setting.[37,77] Additionally, the striatum contains neural tissue with both neuronal cell bodies and myelinated axon bundles, as well as a diversity of glia to enable assessment of graft-host tissue integration.[37]

At 2 weeks post grafting, we detected numerous GFP-positive and HA-positive cells at the striatal injection site across both healthy and stroke conditions (Figures 7B–7H and S7B–S7E). Hb9::GFP-positive cell grafts robustly expressed neurofilament proteins (Figures 7C, 7D, S7D, and S7E) but not the mature neuronal marker, NeuN (Figures 7E–7H). Hb9::GFP-positive cells were negative for the striatal medium spiny neuron marker Darpp-32, suggesting that converted cells maintained their motor neuron identity *in vivo*, even in neural tissue niches where they do not naturally reside (Figures S7F and S7G). While most engrafted cells remained local to the injection site, grafts integrated with host tissue and extended axonal projections several hundred microns into healthy neural tissue (Figures 7F and S7E). There was improved graft survival at small L-NIO strokes compared with healthy tissue, which is consistent with results from previous grafting studies using NPCs (Figures 7I–7K).[78] These data show that our conversion protocol can directly convert donor cells at numbers sufficient for CNS grafting and that grafted iMNs survive at high rates, do not readily adopt host-tissue identity upon transplantation, and integrate with neural tissue in the mouse brain.

DISCUSSION

Cell-fate conversion transforms accessible donor cells into valuable cell types for translational applications, including cell therapies. To support patient access, translational applications require robust and scalable conversion processes to minimize cost and production timelines. Transgene expression of the conversion factors via viral vectors initiate and drive cells through the conversion process. Choice of the viral vector affects the level of transgene expression, transduction rates, and packaging limits. To address these challenges and examine different vectors, we first improved the performance and controllability of our motor neuron conversion cocktail. We used screening to identify optimal, single-transcript encodings of the motor neuron transcription factor module and the high-efficiency module. With these cassettes, we achieved high-yield direct conversion from primary MEFs with the co-delivery of just two viruses. Using these compact cassettes, we were able to compare conversion rates using retrovirus, AAV, and lentivirus. Using the best-performing retroviruses, we then explored how reduced seeding density can dramatically increase conversion yield through proliferation. Using functional assays and transcriptional analysis, we investigated the robustness of our compact, two-genetic cargo conversion system to varying media supplements during conversion to simulate poor neurotrophic support in some *in vivo* environments. Finally, we demonstrate that neurons derived from scalable direct conversion processes can engraft with the mouse CNS.

Given trade-offs between performance and control that exist for delivering transgenes into primary donor cells,[79] how do we rapidly transform primary cells into therapeutically relevant cells at scale? In this work, we set out to use the insight that proliferation history and transcription factor levels act together to drive direct conversion[46] to develop a scalable and robust direct conversion process to obtain functional motor neurons at scale for cell therapies. We first considered how the molecular design of transgenes used in our conversion cocktail impacts performance and design constraints. Minimal sets of transcription factor cocktails for conversion can be condensed into single-transcript cassettes that are efficiently packaged on viral vectors. In exploring the ordering of transcription factors on a polycistronic cassette, we found that we could not predict which designs would perform best as the ordering was not fully correlated with the levels of expression for each factor. However, as we expected, effective designs were distinguished by high expression of Ngn2 at 4 dpi. Thus, for small design spaces, screening remains the best tool to identify optimal designs, as the strict rules of forward design of polycistronic cassettes remain unclear.

Please cite this article in press as: Wang et al., Compact transcription factor cassettes generate functional, engraftable motor neurons by direct conversion, Cell Systems (2025), https://doi.org/10.1016/j.cels.2025.101206

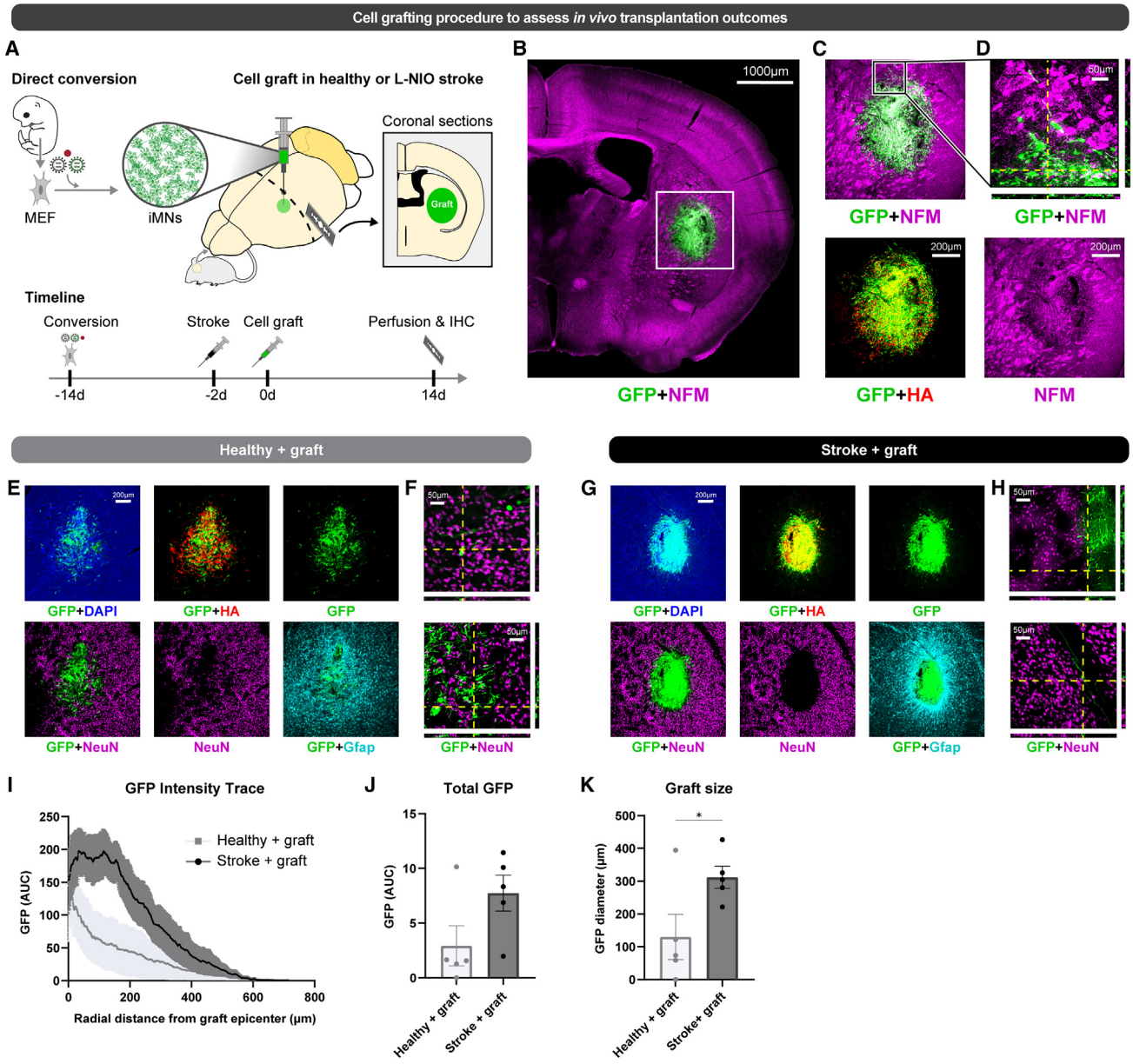

Figure 7. A compact cocktail generates engraftable neurons by direct conversion

(A) Schematic outlining iMN grafting into healthy or stroke mouse brains. Striatal strokes were induced 2 days prior to cell grafting by local injection of L-NIO. iMN graft survival correlates with the time of grafting (Figure S7B).

(B–D) Survey and detailed immunohistochemistry images showing integration of GFP/HA-positive iMNs with striatal stroke lesions. iMNs express the neuronal marker neurofilament (NFM).

(E–H) Coronal sections healthy (E and F) and stroke-induced (G and H) mouse striatums 2 weeks after converted iMN cell graft procedure at various objectives. Sections were imaged for GFP, NFM, NeuN, and glial fibrillary acidic protein (Gfap).

(I) Trace of GFP intensity from graft epicenter radially in healthy + graft (gray square) and stroke + graft (black circle) mouse striatum. Mean is shown ± standard error of mean (s.e.m.).

(J) Quantification of total intensity of GFP-positive grafted iMNs at graft injection site. Quantified by integrating GFP values at 350 μm. Mean is shown ± s.e.m.

(K) Graft size defined at 60th–90th percentile of GFP intensity radially. Mean is shown ± s.e.m; two-tailed t test. Significance summary: $p > 0.05$ (ns) and $^{*}p \leq 0.05$.

While other strategies to vary stoichiometric expression of polycistronic transcripts may help guide design of high-performing, compact cassettes,[80] we find that differences in transcription factor cassette designs become less important with increased proliferation. Potentially, expansion by proliferation may guide more cells into a receptive cell state. Insights from retrospective labeling in conversion of human fibroblasts reveal that cells can move into and out of states that are more receptive to conversion.[45] Further, longitudinal tracking of Oct4 in conversion of human fibroblasts indicates that cells with different Oct4 trajectories

Please cite this article in press as: Wang et al., Compact transcription factor cassettes generate functional, engraftable motor neurons by direct conversion, Cell Systems (2025), https://doi.org/10.1016/j.cels.2025.101206

have different probabilities of generating iPSCs.[49] Future systems that can precisely control and measure all three exogenous transcription factor levels in single cells as they transit through different cell states may help elucidate how cells with different receptivities interpret transcription factor combinations to acquire new cell fates.

While cell lines engineered with inducible transcription factors provide a system for limiting the extrinsic variance associated with viral infection, these systems provide limited flexibility in modifying transcription factor cocktails or require time-consuming initial screening steps.[45,81,82] Achieving rapid, scalable conversion *in vitro* and translatable technologies for *in vivo* conversion requires efficient transgenic systems that induce conversion without the need for extensive cell line engineering. We aimed to develop systems that could be translated to *in vivo* conversion and to adult human fibroblasts.[46] By developing a species-specific high-efficiency module, we increase proliferation in human fibroblasts, which correlates to higher conversion rates and more morphologically mature motor neurons. Unlike iPSC-derived neurons, directly converted neurons retain signatures of aging.[3,6,83] Developing scalable methods for generating neurons from primary adult fibroblasts will support disease modeling in adult-onset neurodegenerative disease such as amyotrophic lateral sclerosis, Parkinson's disease, Huntington's disease, Alzheimer's disease, and frontotemporal dementia. As yet, we do not know if our human high-efficiency conversion module preserves aging signatures or rejuvenates the cell state, which would influence applications in disease modeling and cell therapies. Further, by generating neurons from a greater number of patient-derived cells, direct conversion may provide a more representative survey of cellular diversity within a single patient and avoid clonal bias introduced in clone-based iPSC-derived models.

With compact, singlet-transcript cassettes encoding the conversion and high-efficiency modules, we were able to explore differences in viral expression modalities for conversion. AAVs are commonly used for *in vivo* cell therapies due to their low immunogenic and cytotoxic profiles and ability to express transgenic cargoes without genomic integration. However, we found that AAV delivery to fibroblasts offered poor expression, suggesting AAV would not be well-suited for scalable direct conversion of fibroblasts *in vitro*. Improved delivery modalities such as Sendai viruses[84,85] or RNA-delivery[69,86,87] may offer alternative non-integrating delivery of conversion cassettes. Despite the expression limitations, we demonstrate that AAV-delivered motor neuron transcription factors convert MEFs when co-delivered with retroviral DDR. Thus, targeting different cells with better AAV compatibility or using other delivery modalities may open new avenues for generating neurons *in vivo*. In addition, we show compact cassettes facilitate transcriptional control via small-molecule inducible promoters. Precise control of transgenes during conversion will expand our ability to examine temporal features of transcription factor activity, improve safety profiles, and facilitate improved conversion processes.

Using our highly efficient, two-cargo, retroviral conversion system, we optimized process-level parameters to improve scalability. Given the importance of proliferation in direct conversion,[46,51] we sought to improve conversion rates by decreasing seeding density to encourage proliferation. Lower seeding densities also support scalable conversion processes by decreasing the amount of starting material—including the number of seeded cells and volumes of retrovirus—required to manufacture a specified number of induced neurons. With sparser seeding and more proliferation, we improved conversion yields and purities across cassettes, achieving ultra-high direct conversion yields of greater than 1,000%, representing more than ten iMNs generated per single-cell plated. While altering seeding density to increase proliferation and conversion was effective *in vitro*, this approach will be difficult to translate *in vivo*.

One application for the rapid, large-scale generation of motor neurons by direct conversion is to develop neural cell support for damaged tissue in CNS injuries, where issues such as muscle atrophy can arise from delayed treatment. While the use of integrated oncogenes in our high-efficiency module may limit translational applications, our system is useful to assess the feasibility of sourcing neurons via direct conversion to treat CNS injuries. We demonstrate this potential by showing that motor neurons generated through direct conversion survive *in vivo* upon grafting into the mouse CNS and do not adopt host-tissue identity, opening future studies for *in vivo* conversion and cell therapies.

Key questions remain on the functionality and safety of converted motor neurons for neural cell therapies. Motor neurons develop through both cell-intrinsic and extrinsic cues.[4,71] We observed that the conversion cocktail and media supplements used during *in vitro* conversion affect the functionality and state of converted cells at 14 dpi. However, even without any media supplements, we can generate cells with spontaneous electrical activity. As the *in vivo* environment may provide varying or limited neurotrophic support, our work highlights that electrically active neurons can be generated in the absence of these neurotrophins. Future work can explore how our conversion cocktail may confer neuroprotective properties for other neural regenerative applications.

In profiling the transcriptomes of iMNs generated from different cocktails, we found that our optimized two-virus cocktail leads to a slightly higher fraction of incompletely converted cells compared with our six-factor cocktail at 14 dpi. However, Hb9::GFP-sorted cells display spontaneous electrical activity (Figures 5C and 5D) and do not expand after purification, suggesting the majority of Hb9::GFP-positive cells at 14 dpi are committed to the post-mitotic motor neuron identity.[46] Undesired, proliferative cells represent a common concern across cell sources for neural cell therapies.[23,39,88–91] Eliminating partially converted cells may be important in developing *in vitro* disease models and cell-based therapies.[92] Alternatively, given the power of the transcription factors to drive cells to a post-mitotic fate in the presence of the oncogenes, cocktails of neuronal transcription factors may be useful in arresting growth of transformed cells with minimal impact on non-proliferative cells.

By developing optimized and compact, single-transcript designs, we open the potential for integrating control of conversion with the expanding array of synthetic biology tools for tailoring transgene expression. Beyond targeting specific cell types, precise control of transgenes to induce the conversion of human cells will improve safety and efficacy of gene- and cell-based therapies for regeneration of neural tissue. Though there remain questions on the long-term stability, safety, and efficacy of

directly converted neurons when transplanted *in vivo*, we demonstrate that differentiated motor neurons generated by direct conversion can serve as a well-defined neural cell source for neural regenerative applications.

RESOURCE AVAILABILITY

Lead contact

Requests for further information and resources should be directed to and will be fulfilled by the lead contact, Kate E. Galloway, PhD (katiegal@mit.edu).

Materials availability

Plasmids generated in this study have been deposited to Addgene.

Data and code availability

- The single-cell RNA sequencing data discussed in this publication have been deposited in NCBI's Gene Expression Omnibus (Edgar et al.[93]) and are accessible through GEO Series accession numbers GEO: GSE287783 and GEO: GSE287882. Other data (e.g., flow cytometry data) have been deposited at Zenodo as https://doi.org/10.5281/zenodo.14743950.
- Code is available at https://github.com/GallowayLabMIT/article-engraftable-neurons. The DOI is listed in the key resources table.
- Any additional information required to reanalyze the data reported in this paper is available from the lead contact upon request.

ACKNOWLEDGMENTS

Research reported in this manuscript was supported by the National Institute of General Medical Sciences of the National Institutes of Health under award number R35-GM143033. A.M.B., B.A.L.-D., and N.B.W. are supported by the National Science Foundation Graduate Research Fellowship Program under grant number 1745302. A.M.B. is also supported by the National Cancer Institute under award number F99CA284280. The authors acknowledge the MIT SuperCloud and Lincoln Laboratory Supercomputing Center for providing HPC resources that have contributed to the research results reported within this paper. We thank the Koch Institute's Robert A. Swanson (1969) Biotechnology Center (National Cancer Institute grant P30-CA14051) for technical support, specifically the Flow Cytometry Core Facility. We thank Doug Lauffenberger, Christopher Johnstone, Sneha Kabaria, Emma Peterman, Deon Ploessl, Joji Teves, Mary Ehmann, and especially Kasey Love for feedback on the development of the manuscript.

AUTHOR CONTRIBUTIONS

N.B.W. and B.A.L.-D. performed and analyzed mouse conversion. N.B.W. prepared and analyzed scRNA-seq libraries. N.B.W. and A.M.B. prepared iMNs for cell grafts. H.O.A. performed surgeries, staining, and analysis for cell grafts. K.E.G. and T.M.O. supervised the project. N.B.W., K.E.G., B.A.L.-D., H.O.A., and T.M.O. wrote the manuscript.

DECLARATION OF INTERESTS

The authors declare no competing interests.

STAR★METHODS

Detailed methods are provided in the online version of this paper and include the following:

SUPPLEMENTAL INFORMATION

Supplemental information can be found online at https://doi.org/10.1016/j.cels.2025.101206.

Received: December 28, 2023
Revised: November 7, 2024
Accepted: February 11, 2025
Published: March 13, 2025

REFERENCES

1. Kuang, J., Huang, T., and Pei, D. (2022). The Art of Reprogramming for Regenerative Medicine. Front. Cell Dev. Biol. *10*, 927555. https://doi.org/10.3389/fcell.2022.927555.
2. Wang, H., Yang, Y., Liu, J., and Qian, L. (2021). Direct cell reprogramming: approaches, mechanisms and progress. Nat. Rev. Mol. Cell Biol. *22*, 410–424. https://doi.org/10.1038/s41580-021-00335-z.
3. Herdy, J.R., Traxler, L., Agarwal, R.K., Karbacher, L., Schlachetzki, J.C.M., Boehnke, L., Zangwill, D., Galasko, D., Glass, C.K., Mertens, J., et al. (2022). Increased post-mitotic senescence in aged human neurons is a pathological feature of Alzheimer's disease. Cell Stem Cell *29*, 1637–1652.e6. https://doi.org/10.1016/j.stem.2022.11.010.
4. Ho, R., Sances, S., Gowing, G., Amoroso, M.W., O'Rourke, J.G., Sahabian, A., Wichterle, H., Baloh, R.H., Sareen, D., and Svendsen, C.N. (2016). ALS disrupts spinal motor neuron maturation and aging pathways within gene co-expression networks. Nat. Neurosci. *19*, 1256–1267. https://doi.org/10.1038/nn.4345.
5. Liu, M.-L., Zang, T., and Zhang, C.-L. (2016). Direct Lineage Reprogramming Reveals Disease-Specific Phenotypes of Motor Neurons from Human ALS Patients. Cell Rep. *14*, 115–128. https://doi.org/10.1016/j.celrep.2015.12.018.
6. Mertens, J., Paquola, A.C.M., Ku, M., Hatch, E., Böhnke, L., Ladjevardi, S., McGrath, S., Campbell, B., Lee, H., Herdy, J.R., et al. (2015). Directly Reprogrammed Human Neurons Retain Aging-Associated Transcriptomic Signatures and Reveal Age-Related Nucleocytoplasmic Defects. Cell Stem Cell *17*, 705–718. https://doi.org/10.1016/j.stem.2015.09.001.
7. Assinck, P., Duncan, G.J., Hilton, B.J., Plemel, J.R., and Tetzlaff, W. (2017). Cell transplantation therapy for spinal cord injury. Nat. Neurosci. *20*, 637–647. https://doi.org/10.1038/nn.4541.
8. Björklund, A., and Stenevi, U. (1984). Intracerebral neural implants: neuronal replacement and reconstruction of damaged circuitries. Annu. Rev. Neurosci. *7*, 279–308. https://doi.org/10.1146/annurev.ne.07.030184.001431.
9. Blakemore, W.F., Olby, N.J., and Franklin, R.J. (1995). The use of transplanted glial cells to reconstruct glial environments in the CNS. Brain Pathol. *5*, 443–450. https://doi.org/10.1111/j.1750-3639.1995.tb00623.x.

10. Lindvall, O., Barker, R.A., Brüstle, O., Isacson, O., and Svendsen, C.N. (2012). Clinical Translation of Stem Cells in Neurodegenerative Disorders. Cell Stem Cell *10*, 151–155. https://doi.org/10.1016/j.stem.2012.01.009.

11. Thompson, W. (1890). SUCCESSFUL BRAIN GRAFTING. Science *16*, 78–79. https://doi.org/10.1126/science.ns-16.392.78-a.

12. Björklund, A., Stenevi, U., and Svendgaard, N. (1976). Growth of transplanted monoaminergic neurones into the adult hippocampus along the perforant path. Nature *262*, 787–790. https://doi.org/10.1038/262787a0.

13. Cummings, B.J., Uchida, N., Tamaki, S.J., Salazar, D.L., Hooshmand, M., Summers, R., Gage, F.H., and Anderson, A.J. (2005). Human neural stem cells differentiate and promote locomotor recovery in spinal cord-injured mice. Proc. Natl. Acad. Sci. USA *102*, 14069–14074. https://doi.org/10.1073/pnas.0507063102.

14. Dulin, J.N., Adler, A.F., Kumamaru, H., Poplawski, G.H.D., Lee-Kubli, C., Strobl, H., Gibbs, D., Kadoya, K., Fawcett, J.W., Lu, P., et al. (2018). Injured adult motor and sensory axons regenerate into appropriate organotypic domains of neural progenitor grafts. Nat. Commun. *9*, 84. https://doi.org/10.1038/s41467-017-02613-x.

15. Houlé, J.D., and Reier, P.J. (1988). Transplantation of fetal spinal cord tissue into the chronically injured adult rat spinal cord. J. Comp. Neurol. *269*, 535–547. https://doi.org/10.1002/cne.902690406.

16. Lu, P., Wang, Y., Graham, L., McHale, K., Gao, M., Wu, D., Brock, J., Blesch, A., Rosenzweig, E.S., Havton, L.A., et al. (2012). Long-distance growth and connectivity of neural stem cells after severe spinal cord injury. Cell *150*, 1264–1273. https://doi.org/10.1016/j.cell.2012.08.020.

17. Svendsen, C.N., Caldwell, M.A., Shen, J., ter Borg, M.G., Rosser, A.E., Tyers, P., Karmiol, S., and Dunnett, S.B. (1997). Long-term survival of human central nervous system progenitor cells transplanted into a rat model of Parkinson's disease. Exp. Neurol. *148*, 135–146. https://doi.org/10.1006/exnr.1997.6634.

18. Cao, Q.L., Zhang, Y.P., Howard, R.M., Walters, W.M., Tsoulfas, P., and Whittemore, S.R. (2001). Pluripotent stem cells engrafted into the normal or lesioned adult rat spinal cord are restricted to a glial lineage. Exp. Neurol. *167*, 48–58. https://doi.org/10.1006/exnr.2000.7536.

19. Karimi-Abdolrezaee, S., Eftekharpour, E., Wang, J., Morshead, C.M., and Fehlings, M.G. (2006). Delayed transplantation of adult neural precursor cells promotes remyelination and functional neurological recovery after spinal cord injury. J. Neurosci. *26*, 3377–3389. https://doi.org/10.1523/JNEUROSCI.4184-05.2006.

20. Vroemen, M., Aigner, L., Winkler, J., and Weidner, N. (2003). Adult neural progenitor cell grafts survive after acute spinal cord injury and integrate along axonal pathways. Eur. J. Neurosci. *18*, 743–751. https://doi.org/10.1046/j.1460-9568.2003.02804.x.

21. Mackay-Sim, A., and St John, J.A. (2011). Olfactory ensheathing cells from the nose: clinical application in human spinal cord injuries. Exp. Neurol. *229*, 174–180. https://doi.org/10.1016/j.expneurol.2010.08.025.

22. Bunge, M.B. (2016). Efficacy of Schwann cell transplantation for spinal cord repair is improved with combinatorial strategies. J. Physiol. *594*, 3533–3538. https://doi.org/10.1113/JP271531.

23. Matsuda, R., Yoshikawa, M., Kimura, H., Ouji, Y., Nakase, H., Nishimura, F., Nonaka, J.-I., Toriumi, H., Yamada, S., Nishiofuku, M., et al. (2009). Cotransplantation of Mouse Embryonic Stem Cells and Bone Marrow Stromal Cells following Spinal Cord Injury Suppresses Tumor Development. Cell Transplant. *18*, 39–54. https://doi.org/10.3727/096368909788237122.

24. Ritfeld, G.J., Patel, A., Chou, A., Novosat, T.L., Castillo, D.G., Roos, R.A.C., and Oudega, M. (2015). The role of brain-derived neurotrophic factor in bone marrow stromal cell-mediated spinal cord repair. Cell Transplant. *24*, 2209–2220. https://doi.org/10.3727/096368915X686201.

25. Steinberg, G.K., Kondziolka, D., Wechsler, L.R., Lunsford, L.D., Coburn, M.L., Billigen, J.B., Kim, A.S., Johnson, J.N., Bates, D., King, B., et al. (2016). Clinical Outcomes of Transplanted Modified Bone Marrow-Derived Mesenchymal Stem Cells in Stroke: A Phase 1/2a Study. Stroke *47*, 1817–1824. https://doi.org/10.1161/STROKEAHA.116.012995.

26. Akhtar, A.A., Gowing, G., Kobritz, N., Savinoff, S.E., Garcia, L., Saxon, D., Cho, N., Kim, G., Tom, C.M., Park, H., et al. (2018). Inducible Expression of GDNF in Transplanted iPSC-Derived Neural Progenitor Cells. Stem Cell Rep. *10*, 1696–1704. https://doi.org/10.1016/j.stemcr.2018.03.024.

27. Kadoya, K., Lu, P., Nguyen, K., Lee-Kubli, C., Kumamaru, H., Yao, L., Knackert, J., Poplawski, G., Dulin, J.N., Strobl, H., et al. (2016). Spinal cord reconstitution with homologous neural grafts enables robust corticospinal regeneration. Nat. Med. *22*, 479–487. https://doi.org/10.1038/nm.4066.

28. Keirstead, H.S., Nistor, G., Bernal, G., Totoiu, M., Cloutier, F., Sharp, K., and Steward, O. (2005). Human Embryonic Stem Cell-Derived Oligodendrocyte Progenitor Cell Transplants Remyelinate and Restore Locomotion after Spinal Cord Injury. J. Neurosci. *25*, 4694–4705. https://doi.org/10.1523/JNEUROSCI.0311-05.2005.

29. Kokaia, Z., Llorente, I.L., and Carmichael, S.T. (2018). Customized Brain Cells for Stroke Patients Using Pluripotent Stem Cells. Stroke *49*, 1091–1098. https://doi.org/10.1161/STROKEAHA.117.018291.

30. Nori, S., Okada, Y., Yasuda, A., Tsuji, O., Takahashi, Y., Kobayashi, Y., Fujiyoshi, K., Koike, M., Uchiyama, Y., Ikeda, E., et al. (2011). Grafted human-induced pluripotent stem-cell–derived neurospheres promote motor functional recovery after spinal cord injury in mice. Proc. Natl. Acad. Sci. USA *108*, 16825–16830. https://doi.org/10.1073/pnas.1108077108.

31. Palma-Tortosa, S., Tornero, D., Grønning Hansen, M., Monni, E., Hajy, M., Kartsivadze, S., Aktay, S., Tsupykov, O., Parmar, M., Deisseroth, K., et al. (2020). Activity in grafted human iPS cell-derived cortical neurons integrated in stroke-injured rat brain regulates motor behavior. Proc. Natl. Acad. Sci. USA *117*, 9094–9100. https://doi.org/10.1073/pnas.2000690117.

32. Sareen, D., Gowing, G., Sahabian, A., Staggenborg, K., Paradis, R., Avalos, P., Latter, J., Ornelas, L., Garcia, L., and Svendsen, C.N. (2014). Human induced pluripotent stem cells are a novel source of neural progenitor cells (iNPCs) that migrate and integrate in the rodent spinal cord. J. Comp. Neurol. *522*, 2707–2728. https://doi.org/10.1002/cne.23578.

33. Fischer, I., Dulin, J.N., and Lane, M.A. (2020). Transplanting neural progenitor cells to restore connectivity after spinal cord injury. Nat. Rev. Neurosci. *21*, 366–383. https://doi.org/10.1038/s41583-020-0314-2.

34. Rosenzweig, E.S., Brock, J.H., Lu, P., Kumamaru, H., Salegio, E.A., Kadoya, K., Weber, J.L., Liang, J.J., Moseanko, R., Hawbecker, S., et al. (2018). Restorative effects of human neural stem cell grafts on the primate spinal cord. Nat. Med. *24*, 484–490. https://doi.org/10.1038/nm.4502.

35. Aceves, M., Tucker, A., Chen, J., Vo, K., Moses, J., Amar Kumar, P., Thomas, H., Miranda, D., Dampf, G., Dietz, V., et al. (2023). Developmental stage of transplanted neural progenitor cells influences anatomical and functional outcomes after spinal cord injury in mice. Commun. Biol. *6*, 544. https://doi.org/10.1038/s42003-023-04893-0.

36. Nguyen, H.X., Hooshmand, M.J., Saiwai, H., Maddox, J., Salehi, A., Lakatos, A., Nishi, R.A., Salazar, D., Uchida, N., and Anderson, A.J. (2017). Systemic Neutrophil Depletion Modulates the Migration and Fate of Transplanted Human Neural Stem Cells to Rescue Functional Repair. J. Neurosci. *37*, 9269–9287. https://doi.org/10.1523/JNEUROSCI.2785-16.2017.

37. O'Shea, T.M., Ao, Y., Wang, S., Wollenberg, A.L., Kim, J.H., Ramos Espinoza, R.A., Czechanski, A., Reinholdt, L.G., Deming, T.J., and Sofroniew, M.V. (2022). Lesion environments direct transplanted neural progenitors towards a wound repair astroglial phenotype in mice. Nat. Commun. *13*, 5702. https://doi.org/10.1038/s41467-022-33382-x.

38. Piltti, K.M., Salazar, D.L., Uchida, N., Cummings, B.J., and Anderson, A.J. (2013). Safety of epicenter versus intact parenchyma as a transplantation site for human neural stem cells for spinal cord injury therapy. Stem Cells Transl. Med. *2*, 204–216. https://doi.org/10.5966/sctm.2012-0110.

39. Steward, O., Sharp, K.G., Yee, K.M., Hatch, M.N., and Bonner, J.F. (2014). Characterization of Ectopic Colonies That Form in Widespread Areas of the Nervous System with Neural Stem Cell Transplants into the Site of a Severe Spinal Cord Injury. J. Neurosci. *34*, 14013–14021. https://doi.org/10.1523/JNEUROSCI.3066-14.2014.

40. Darsalia, V., Allison, S.J., Cusulin, C., Monni, E., Kuzdas, D., Kallur, T., Lindvall, O., and Kokaia, Z. (2011). Cell Number and Timing of Transplantation Determine Survival of Human Neural Stem Cell Grafts in Stroke-Damaged Rat Brain. J. Cereb. Blood Flow Metab. *31*, 235–242. https://doi.org/10.1038/jcbfm.2010.81.

41. Biddy, B.A., Kong, W., Kamimoto, K., Guo, C., Waye, S.E., Sun, T., and Morris, S.A. (2018). Single-cell mapping of lineage and identity in direct reprogramming. Nature *564*, 219–224. https://doi.org/10.1038/s41586-018-0744-4.

42. Emert, B.L., Cote, C.J., Torre, E.A., Dardani, I.P., Jiang, C.L., Jain, N., Shaffer, S.M., and Raj, A. (2021). Variability within rare cell states enables multiple paths toward drug resistance. Nat. Biotechnol. *39*, 865–876. https://doi.org/10.1038/s41587-021-00837-3.

43. Gutierrez, C., Al'Khafaji, A.M., Brenner, E., Johnson, K.E., Gohil, S.H., Lin, Z., Knisbacher, B.A., Durrett, R.E., Li, S., Parvin, S., et al. (2021). Multifunctional barcoding with ClonMapper enables high-resolution study of clonal dynamics during tumor evolution and treatment. Nat. Cancer *2*, 758–772. https://doi.org/10.1038/s43018-021-00222-8.

44. Liu, W., Saelens, W., Rainer, P., Biočanin, M., Gardeux, V., Gralak, A., van Mierlo, G., Russeil, J., Liu, T., Chen, W., et al. (2024). Dissecting reprogramming heterogeneity at single-cell resolution using scTF-seq. Preprint at bioRxiv. https://doi.org/10.1101/2024.01.30.577921.

45. Jain, N., Goyal, Y., Dunagin, M.C., Cote, C.J., Mellis, I.A., Emert, B., Jiang, C.L., Dardani, I.P., Reffsin, S., Arnett, M., et al. (2024). Retrospective identification of cell-intrinsic factors that mark pluripotency potential in rare somatic cells. Cell Syst. *15*, 109–133.e10. https://doi.org/10.1016/j.cels.2024.01.001.

46. Wang, N.B., Lende-Dorn, B.A., Beitz, A.M., Han, P., Adewumi, H.O., O'Shea, T.M., and Galloway, K.E. (2025). Proliferation history and transcription factor levels drive direct conversion to motor neurons. Cell Syst. 16. https://doi.org/10.1016/j.cels.2025.101205.

47. Kabaria, S.R., Bae, Y., Ehmann, M.E., Beitz, A.M., Lende-Dorn, B.A., Peterman, E.L., Love, K.S., Ploessl, D.S., and Galloway, K.E. (2024). Programmable promoter editing for precise control of transgene expression. Preprint at bioRxiv. https://doi.org/10.1101/2024.06.19.599813.

48. Love, K.S., Johnstone, C.P., Peterman, E.L., Gaglione, S., and Galloway, K.E. (2024). Model-guided design of microRNA-based gene circuits supports precise dosage of transgenic cargoes into diverse primary cells. Preprint at bioRxiv. https://doi.org/10.1101/2024.06.25.600629.

49. Ilia, K., Shakiba, N., Bingham, T., Jones, R.D., Kaminski, M.M., Aravera, E., Bruno, S., Palacios, S., Weiss, R., Collins, J.J., et al. (2023). Synthetic genetic circuits to uncover the OCT4 trajectories of successful reprogramming of human fibroblasts. Sci. Adv. *9*, eadg8495. https://doi.org/10.1126/sciadv.adg8495.

50. Wang, N.B., Beitz, A.M., and Galloway, K.E. (2020). Engineering cell fate: Applying synthetic biology to cellular reprogramming. Curr. Opin. Syst. Biol. *24*, 18–31. https://doi.org/10.1016/j.coisb.2020.09.002.

51. Babos, K.N., Galloway, K.E., Kisler, K., Zitting, M., Li, Y., Shi, Y., Quintino, B., Chow, R.H., Zlokovic, B.V., and Ichida, J.K. (2019). Mitigating Antagonism between Transcription and Proliferation Allows Near-Deterministic Cellular Reprogramming. Cell Stem Cell *25*, 486–500.e9. https://doi.org/10.1016/j.stem.2019.08.005.

52. Wichterle, H., Lieberam, I., Porter, J.A., and Jessell, T.M. (2002). Directed Differentiation of Embryonic Stem Cells into Motor Neurons. Cell *110*, 385–397. https://doi.org/10.1016/S0092-8674(02)00835-8.

53. Mizuguchi, H., Xu, Z., Ishii-Watabe, A., Uchida, E., and Hayakawa, T. (2000). IRES-Dependent Second Gene Expression Is Significantly Lower Than Cap-Dependent First Gene Expression in a Bicistronic Vector. Mol. Ther. *1*, 376–382. https://doi.org/10.1006/mthe.2000.0050.

54. Carey, B.W., Markoulaki, S., Hanna, J.H., Faddah, D.A., Buganim, Y., Kim, J., Ganz, K., Steine, E.J., Cassady, J.P., Creyghton, M.P., et al. (2011). Reprogramming Factor Stoichiometry Influences the Epigenetic State and Biological Properties of Induced Pluripotent Stem Cells. Cell Stem Cell *9*, 588–598. https://doi.org/10.1016/j.stem.2011.11.003.

55. Kim, J.H., Lee, S.-R., Li, L.-H., Park, H.-J., Park, J.-H., Lee, K.Y., Kim, M.-K., Shin, B.A., and Choi, S.-Y. (2011). High Cleavage Efficiency of a 2A Peptide Derived from Porcine Teschovirus-1 in Human Cell Lines, Zebrafish and Mice. PLoS One *6*, e18556. https://doi.org/10.1371/journal.pone.0018556.

56. Liu, Z., Chen, O., Wall, J.B.J., Zheng, M., Zhou, Y., Wang, L., Vaseghi, H.R., Qian, L., and Liu, J. (2017). Systematic comparison of 2A peptides for cloning multi-genes in a polycistronic vector. Sci. Rep. *7*, 2193. https://doi.org/10.1038/s41598-017-02460-2.

57. Rosa, F.F., Pires, C.F., Kurochkin, I., Ferreira, A.G., Gomes, A.M., Palma, L.G., Shaiv, K., Solanas, L., Azenha, C., Papatsenko, D., et al. (2018). Direct reprogramming of fibroblasts into antigen-presenting dendritic cells. Sci. Immunol. *3*, eaau4292. https://doi.org/10.1126/sciimmunol.aau4292.

58. Wang, L., Liu, Z., Yin, C., Asfour, H., Chen, O., Li, Y., Bursac, N., Liu, J., and Qian, L. (2015). Stoichiometry of Gata4, Mef2c, and Tbx5 Influences the Efficiency and Quality of Induced Cardiac Myocyte Reprogramming. Circ. Res. *116*, 237–244. https://doi.org/10.1161/CIRCRESAHA.116.305547.

59. Zhu, X., Ricci-Tam, C., Hager, E.R., and Sgro, A.E. (2023). Self-cleaving peptides for expression of multiple genes in Dictyostelium discoideum. PLoS One *18*, e0281211. https://doi.org/10.1371/journal.pone.0281211.

60. Mazzoni, E.O., Mahony, S., Closser, M., Morrison, C.A., Nedelec, S., Williams, D.J., An, D., Gifford, D.K., and Wichterle, H. (2013). Synergistic binding of transcription factors to cell-specific enhancers programs motor neuron identity. Nat. Neurosci. *16*, 1219–1227. https://doi.org/10.1038/nn.3467.

61. Lee, S., Cuvillier, J.M., Lee, B., Shen, R., Lee, J.W., and Lee, S.-K. (2012). Fusion protein Isl1–Lhx3 specifies motor neuron fate by inducing motor neuron genes and concomitantly suppressing the interneuron programs. Proc. Natl. Acad. Sci. USA *109*, 3383–3388. https://doi.org/10.1073/pnas.1114515109.

62. Wang, D., Tai, P.W.L., and Gao, G. (2019). Adeno-associated virus vector as a platform for gene therapy delivery. Nat. Rev. Drug Discov. *18*, 358–378. https://doi.org/10.1038/s41573-019-0012-9.

63. Balaji, S., Dhamija, Y., Leung, A., Le, L., Marsh, E., Crombleholme, T.M., and Keswani, S.G. (2013). Transduction Efficiency of Pseudotyped Adeno-Associated Viral Vectors for Gene Transfer in Dermal Fibroblasts to Modulate Wound Healing. J. Surg. Res. *179*, 260–261. https://doi.org/10.1016/j.jss.2012.10.498.

64. Ellis, B.L., Hirsch, M.L., Barker, J.C., Connelly, J.P., Steininger, R.J., and Porteus, M.H. (2013). A survey of ex vivo/in vitro transduction efficiency of mammalian primary cells and cell lines with Nine natural adeno-associated virus (AAV1-9) and one engineered adeno-associated virus serotype. Virol. J. *10*, 74. https://doi.org/10.1186/1743-422X-10-74.

65. Weltner, J., Anisimov, A., Alitalo, K., Otonkoski, T., and Trokovic, R. (2012). Induced Pluripotent Stem Cell Clones Reprogrammed via Recombinant Adeno-Associated Virus-Mediated Transduction Contain Integrated Vector Sequences. J. Virol. *86*, 4463–4467. https://doi.org/10.1128/JVI.06302-11.

66. Zengel, J., Wang, Y.X., Seo, J.W., Ning, K., Hamilton, J.N., Wu, B., Raie, M., Holbrook, C., Su, S., Clements, D.R., et al. (2023). Hardwiring tissue-specific AAV transduction in mice through engineered receptor expression. Nat. Methods *20*, 1070–1081. https://doi.org/10.1038/s41592-023-01896-x.

67. Keppler, A., Gendreizig, S., Gronemeyer, T., Pick, H., Vogel, H., and Johnsson, K. (2003). A general method for the covalent labeling of fusion proteins with small molecules in vivo. Nat. Biotechnol. *21*, 86–89. https://doi.org/10.1038/nbt765.

68. Qin, J.Y., Zhang, L., Clift, K.L., Hulur, I., Xiang, A.P., Ren, B.-Z., and Lahn, B.T. (2010). Systematic Comparison of Constitutive Promoters and the Doxycycline-Inducible Promoter. PLoS One *5*, e10611. https://doi.org/10.1371/journal.pone.0010611.

69. Kogut, I., McCarthy, S.M., Pavlova, M., Astling, D.P., Chen, X., Jakimenko, A., Jones, K.L., Getahun, A., Cambier, J.C., Pasmooij, A.M.G., et al. (2018).

High-efficiency RNA-based reprogramming of human primary fibroblasts. Nat. Commun. *9*, 745. https://doi.org/10.1038/s41467-018-03190-3.

70. Son, E.Y., Ichida, J.K., Wainger, B.J., Toma, J.S., Rafuse, V.F., Woolf, C.J., and Eggan, K. (2011). Conversion of mouse and human fibroblasts into functional spinal motor neurons. Cell Stem Cell *9*, 205–218. https://doi.org/10.1016/j.stem.2011.07.014.
71. Patel, T., Hammelman, J., Aziz, S., Jang, S., Closser, M., Michaels, T.L., Blum, J.A., Gifford, D.K., and Wichterle, H. (2022). Transcriptional dynamics of murine motor neuron maturation in vivo and in vitro. Nat. Commun. *13*, 5427. https://doi.org/10.1038/s41467-022-33022-4.
72. Dana, H., Mohar, B., Sun, Y., Narayan, S., Gordus, A., Hasseman, J.P., Tsegaye, G., Holt, G.T., Hu, A., Walpita, D., et al. (2016). Sensitive red protein calcium indicators for imaging neural activity. eLife *5*, e12727. https://doi.org/10.7554/eLife.12727.
73. Álvarez, Z., Ortega, J.A., Sato, K., Sasselli, I.R., Kolberg-Edelbrock, A.N., Qiu, R., Marshall, K.A., Nguyen, T.P., Smith, C.S., Quinlan, K.A., et al. (2023). Artificial extracellular matrix scaffolds of mobile molecules enhance maturation of human stem cell-derived neurons. Cell Stem Cell *30*, 219–238.e14. https://doi.org/10.1016/j.stem.2022.12.010.
74. Tutukova, S., Tarabykin, V., and Hernandez-Miranda, L.R. (2021). The Role of Neurod Genes in Brain Development, Function, and Disease. Front. Mol. Neurosci. *14*, 662774. https://doi.org/10.3389/fnmol.2021.662774.
75. Tabar, V., and Studer, L. (2014). Pluripotent stem cells in regenerative medicine: challenges and recent progress. Nat. Rev. Genet. *15*, 82–92. https://doi.org/10.1038/nrg3563.
76. Ceto, S., Sekiguchi, K.J., Takashima, Y., Nimmerjahn, A., and Tuszynski, M.H. (2020). Neural Stem Cell Grafts Form Extensive Synaptic Networks that Integrate with Host Circuits after Spinal Cord Injury. Cell Stem Cell *27*, 430–440.e5. https://doi.org/10.1016/j.stem.2020.07.007.
77. Zhang, Y., Pak, C., Han, Y., Ahlenius, H., Zhang, Z., Chanda, S., Marro, S., Patzke, C., Acuna, C., Covy, J., et al. (2013). Rapid Single-Step Induction of Functional Neurons from Human Pluripotent Stem Cells. Neuron *78*, 785–798. https://doi.org/10.1016/j.neuron.2013.05.029.
78. Adewumi, H.O., Berniac, G.I., McCarthy, E.A., and O'Shea, T.M. (2024). Ischemic and hemorrhagic stroke lesion environments differentially alter the glia repair potential of neural progenitor cell and immature astrocyte grafts. Exp. Neurol. *374*, 114692. https://doi.org/10.1016/j.expneurol.2024.114692.
79. Peterman, E.L., Ploessl, D.S., and Galloway, K.E. (2024). Accelerating Diverse Cell-Based Therapies Through Scalable Design. Annu. Rev. Chem. Biomol. Eng. *15*, 267–292. https://doi.org/10.1146/annurev-chembioeng-100722-121610.
80. Duan, M., Dev, I., Lu, A., Ayrapetyan, G., You, M.Y., and Shapiro, M.G. (2024). SEMPER: Stoichiometric expression of mRNA polycistrons by eukaryotic ribosomes for compact, ratio-tunable multi-gene expression. Cell Syst. *15*, 597–609.e4. https://doi.org/10.1016/j.cels.2024.06.001.
81. Blanch-Asensio, A., Ploessl, D.S., Wang, N.B., Mummery, C.L., Galloway, K.E., and Davis, R.P. (2024). STRAIGHT-IN Dual: a platform for dual, single-copy integrations of DNA payloads and gene circuits into human induced pluripotent stem cells. Preprint at bioRxiv. https://doi.org/10.1101/2024.10.17.616637.
82. Elbaz, J., Puri, M.C., Faiz, M., Bang, K.W.A., Nguyen, L., Makovoz, B., Gertsenstein, M., Hussein, S.M.I., Zandstra, P.W., Briollais, L., et al. (2022). Highly efficient reprogrammable mouse lines with integrated reporters to track the route to pluripotency. Proc. Natl. Acad. Sci. USA *119*, e2207824119. https://doi.org/10.1073/pnas.2207824119.
83. Mertens, J., Herdy, J.R., Traxler, L., Schafer, S.T., Schlachetzki, J.C.M., Böhnke, L., Reid, D.A., Lee, H., Zangwill, D., Fernandes, D.P., et al. (2021). Age-dependent instability of mature neuronal fate in induced neurons from Alzheimer's patients. Cell Stem Cell *28*, 1533–1548.e6. https://doi.org/10.1016/j.stem.2021.04.004.
84. Kunitomi, A., Hirohata, R., Arreola, V., Osawa, M., Kato, T.M., Nomura, M., Kawaguchi, J., Hara, H., Kusano, K., Takashima, Y., et al. (2022). Improved Sendai viral system for reprogramming to naive pluripotency. Cell Rep. Methods *2*, 100317. https://doi.org/10.1016/j.crmeth.2022.100317.
85. Miyamoto, K., Akiyama, M., Tamura, F., Isomi, M., Yamakawa, H., Sadahiro, T., Muraoka, N., Kojima, H., Haginiwa, S., Kurotsu, S., et al. (2018). Direct In Vivo Reprogramming with Sendai Virus Vectors Improves Cardiac Function after Myocardial Infarction. Cell Stem Cell *22*, 91–103.e5. https://doi.org/10.1016/j.stem.2017.11.010.
86. Warren, L., Manos, P.D., Ahfeldt, T., Loh, Y.-H., Li, H., Lau, F., Ebina, W., Mandal, P.K., Smith, Z.D., Meissner, A., et al. (2010). Highly Efficient Reprogramming to Pluripotency and Directed Differentiation of Human Cells with Synthetic Modified mRNA. Cell Stem Cell *7*, 618–630. https://doi.org/10.1016/j.stem.2010.08.012.
87. Yoshioka, N., Gros, E., Li, H.-R., Kumar, S., Deacon, D.C., Maron, C., Muotri, A.R., Chi, N.C., Fu, X.-D., Yu, B.D., et al. (2013). Efficient Generation of Human iPSCs by a Synthetic Self-Replicative RNA. Cell Stem Cell *13*, 246–254. https://doi.org/10.1016/j.stem.2013.06.001.
88. Fernandopulle, M.S., Prestil, R., Grunseich, C., Wang, C., Gan, L., and Ward, M.E. (2018). Transcription Factor-Mediated Differentiation of Human iPSCs into Neurons. Curr. Protoc. Cell Biol. *79*, e51. https://doi.org/10.1002/cpcb.51.
89. Nguyen, T.D., Chooi, W.H., Jeon, H., Chen, J., Tan, J., Roxby, D.N., Lee, C.Y.-P., Ng, S.-Y., Chew, S.Y., and Han, J. (2024). Label-Free and High-Throughput Removal of Residual Undifferentiated Cells From iPSC-Derived Spinal Cord Progenitor Cells. Stem Cells Transl. Med. *13*, 387–398. https://doi.org/10.1093/stcltm/szae002.
90. Tieng, V., Cherpin, O., Gutzwiller, E., Zambon, A.C., Delgado, C., Salmon, P., Dubois-Dauphin, M., and Krause, K.-H. (2016). Elimination of proliferating cells from CNS grafts using a Ki67 promoter-driven thymidine kinase. Mol. Ther. Methods Clin. Dev. *6*, 16069. https://doi.org/10.1038/mtm.2016.69.
91. Locatelli, M., Delhaes, F., Cherpin, O., Black, M.E., Carnesecchi, S., Preynat-Seauve, O., Hibaoui, Y., and Krause, K.-H. (2022). Optimization of Thymidine Kinase-Based Safety Switch for Neural Cell Therapy. Cells *11*, 502. https://doi.org/10.3390/cells11030502.
92. Chanda, S., Ang, C.E., Davila, J., Pak, C., Mall, M., Lee, Q.Y., Ahlenius, H., Jung, S.W., Südhof, T.C., and Wernig, M. (2014). Generation of Induced Neuronal Cells by the Single Reprogramming Factor ASCL1. Stem Cell Rep. *3*, 282–296. https://doi.org/10.1016/j.stemcr.2014.05.020.
93. Edgar, R., Domrachev, M., and Lash, A.E. (2002). Gene Expression Omnibus: NCBI gene expression and hybridization array data repository. Nucleic Acids Res *30*, 207–210. https://doi.org/10.1093/nar/30.1.207.
94. Davis-Dusenbery, B.N., Williams, L.A., Klim, J.R., and Eggan, K. (2014). How to make spinal motor neurons. Development *141*, 491–501. https://doi.org/10.1242/dev.097410.
95. Delile, J., Rayon, T., Melchionda, M., Edwards, A., Briscoe, J., and Sagner, A. (2019). Single cell transcriptomics reveals spatial and temporal dynamics of gene expression in the developing mouse spinal cord. Development *146*, dev173807. https://doi.org/10.1242/dev.173807.
96. Ichida, J.K., Staats, K.A., Davis-Dusenbery, B.N., Clement, K., Galloway, K.E., Babos, K.N., Shi, Y., Son, E.Y., Kiskinis, E., Atwater, N., et al. (2018). Comparative genomic analysis of embryonic, lineage-converted and stem cell-derived motor neurons. Development *145*, dev168617. https://doi.org/10.1242/dev.168617.
97. Stifani, N. (2014). Motor neurons and the generation of spinal motor neuron diversity. Front. Cell. Neurosci. *8*, 293. https://doi.org/10.3389/fncel.2014.00293.

Please cite this article in press as: Wang et al., Compact transcription factor cassettes generate functional, engraftable motor neurons by direct conversion, Cell Systems (2025), https://doi.org/10.1016/j.cels.2025.101206

STAR★METHODS

KEY RESOURCES TABLE

REAGENT or RESOURCE	SOURCE	IDENTIFIER
Antibodies		
mouse anti-Ngn2	Santa Cruz	Cat# sc-293430
mouse anti-Isl1	DHSB	Cat# 40.2D6; RRID:AB_528315
mouse anti-Lhx3	DHSB	Cat#67.4E12; RRID:AB_2135805
mouse anti-Hemagglutinin (HA)	Biolegend	Cat#901501; RRID:AB_2565006
mouse anti-TUBB3	Biolegend	Cat#801202; RRID:AB_10063408
rabbit anti-MAP2	Cell Signaling Technology	Cat# #4542; RRID:AB_10693782
goat anti-Choline Acetyltransferase (ChAT)	MilliporeSigma	Cat# AB144P; RRID:AB_2079751
mouse anti-β-Actin	Cell Signaling Technology	Cat#3700; RRID:AB_2242334
rabbit anti-Ras (G12V Mutant Specific)	Cell Signaling Technology	Cat#14412; RRID:AB_2714031
rabbit anti-p53	Cell Signaling Technology	Cat#32532; RRID:AB_2757821
rabbit anti-Hemagglutinin (HA)	Sigma	Cat#H6908; RRID:AB_260070
goat anti-Hemagglutinin (HA)	Novus	Cat#NB600-362; RRID:AB_10124937
rat anti-Gfap	Thermofisher	Cat#13-0300; RRID:AB_86543
guinea pig anti-NeuN	Synaptic Systems	Cat#266 004; RRID:AB_2619988
rabbit anti-Neurofilament M (NFM)	Millipore Sigma	Cat#AB1987; RRID:AB_91201
chicken anti-GFP	Abcam	Cat#ab13970; RRID:AB_300798
rabbit anti-GFP	Abcam	Cat#ab290; RRID:AB_303395
rabbit anti-DARPP-32	Cell Signaling	Cat#2306; RRID:AB_823479
donkey anti-mouse Alexa Fluor 647	Invitrogen	Cat# A-31571; RRID: AB_162542
donkey anti-rabbit Alexa Fluor 594	Invitrogen	Cat# A-21207; RRID: AB_141637
donkey anti-rabbit Alexa Fluor 647	Invitrogen	Cat# A-31573; RRID:AB_2536183
goat anti-mouse Alexa Fluor 488	Jackson ImmunoResearch Labs	Cat# 115-546-146; RRID:AB_2338868
donkey anti-goat Alexa Fluor 647	Jackson ImmunoResearch Labs	Cat# 705-605-147; RRID:AB_2340437
goat anti-mouse IgG H&L (HRP)	Abcam	Cat#ab205719; RRID:AB_2755049
goat anti-rabbit IgG H&L (HRP)	Abcam	Cat#ab6721; RRID:AB_955447
Chemicals, peptides, and recombinant proteins		
RepSox (TGF-β inhibitor)	Selleck Chemicals	Cat#S7223
Recombinant Human BDNF Protein	R&D Systems	Cat#248-BDB-050
Recombinant Human CNTF Protein	R&D Systems	Cat#257-NT-050
Recombinant Human GDNF Protein	R&D Systems	Cat#212-GD-050
Recombinant Human Protein FGF-Basic (154 a.a.)	Peprotech	Cat#100-18B
(+)-Aphidicolin	Cayman Chemicals	Cat#38966-21-1
DAPI	Tocris	Cat#5748
DMEM	Genesee Scientific	Cat#25-500
Fetal Bovine Serum	Genesee Scientific	Cat#25-514H
HEPES	Sigma-Aldrich	Cat#H3375
Hexadimethrine bromide	Sigma-Aldrich	Cat#H9268
DMEM/F-12, no glutamine	Thermo Scientific	Cat#21-331-020
B-27 Supplement (50X), serum free	Thermo Scientific	Cat#17-504-044
N-2 Supplement (100X)	Thermo Scientific	Cat#17-502-048
GlutaMAX Supplement	Thermo Scientific	Cat#35-050-061
MEM Non Essential Amino Acids Solution (100X)	Thermo Scientific	Cat#11-140-050

(*Continued on next page*)

Please cite this article in press as: Wang et al., Compact transcription factor cassettes generate functional, engraftable motor neurons by direct conversion, Cell Systems (2025), https://doi.org/10.1016/j.cels.2025.101206

Continued

REAGENT or RESOURCE	SOURCE	IDENTIFIER
DNase	Worthington Biochemical	Cat#9003-98-9
Papain	Worthington Biochemical	Cat#9001-73-4
Penicillin-Streptomycin (10,000 U/mL)	Thermo Scientific	Cat#15-140-122
Bovine Serum Albumin	Sigma-Aldrich	Cat#A2058
Laminin	Corning	Cat#354232
Gelatin	Sigma-Aldrich	Cat#G1890
Lenti-X Concentrator	Takara Bio	Cat#631232
SNAP-Cell 647-SiR	New England Biolabs (NEB)	Cat#S9105S
CellAdhere Laminin-521	STEMCELL Technologies	Cat#200-0117
Poly(ethyleneimine)	Sigma-Aldrich	Cat#P3143
BrainPhys Neuronal Medium	STEMCELL Technologies	Cat#05790
L-NIO (N5-(1-Iminoethyl)-L-ornithine)	Sigma-Aldrich	Cat#400600
Critical commercial assays		
CellTrace Violet Cell Proliferation Kit, for flow cytometry	Thermo Scientific	Cat#C34557
CellTrace Far Red Cell Proliferation Kit, for flow cytometry	Thermo Scientific	Cat#C34564
SuperSignal West Femto Maximum Sensitivity Substrate	Thermo Scientific	Cat#34096
iBlot 2 Transfer Stacks	Thermo Scientific	Cat#IB24001
Zombie NIR Fixable Viability Kit	BioLegend	Cat#423105
Deposited data		
Raw and analyzed data	This study	Zenodo: https://doi.org/10.5281/zenodo.14743950
scRNA-seq of LNI+DDRR	This study	GEO: GSE287783
scRNA-seq of embMN, MEFs, 6F+DDRR	This study	GEO: GSE287882
Mouse reference genome, GRCm39	Genome Reference Consortium	N/A
Experimental models: Cell lines		
Human: HEK293T	ATCC	Cat#CRL-3216
Human: Plat-E Retroviral Packaging Cell Line	Cell Biolabs, Inc.	Cat#RV-101
Experimental models: Organisms/strains		
Mouse: C57BL/6J	The Jackson Laboratory	Cat#000664, RRID:IMSR_JAX:000664
Mouse: B6.Cg-Tg(Hlxb9-GFP)1Tmj/J	The Jackson Laboratory	Cat#005029, RRID:IMSR_JAX:005029
Recombinant DNA		
pMXs-NIL	This study	Addgene #233154
pMXs-HRAS(G12V)-IRES-p53DD	This study	Addgene #233185
pENTR-HRAS(G12V)-IRES-p53DD	This study	Addgene #233186
pMXs-p53DD-IRES-HRAS(G12V)	This study	Addgene #233187
pENTR-p53DD-IRES-HRAS(G12V)	This study	Addgene #233188
pMXs-mNgn2-x3HA	This study	Addgene #233189
pMXs-mNgn2-x3FLAG	This study	Addgene #233190
pMXs-mNgn2-x1HA	This study	Addgene #233191
pMXs-NIL (with mNgn2x3HA)	This study	Addgene #233192
pMXs-NLI (with mNgn2x3HA)	This study	Addgene #233193
pMXs-LIN (with mNgn2x3HA)	This study	Addgene #233194
pMXs-LNI (with mNgn2x3HA)	This study	Addgene #233195
pMXs-ILN (with mNgn2x3HA)	This study	Addgene #233196
pMXs-INL (with mNgn2x3HA)	This study	Addgene #233197
pMXs-HRAS(G12V)-IRES-SNAP-p53DD	This study	Addgene #233198

(*Continued on next page*)

Continued

REAGENT or RESOURCE	SOURCE	IDENTIFIER
pENTR-HRAS(G12V)-IRES-SNAP-p53DD	This study	Addgene #233199
pMXs-SNAP-p53DD-IRES-HRAS(G12V)	This study	Addgene #233200
pENTR-SNAP-p53DD-IRES-HRAS(G12V)	This study	Addgene #233201
pMXs-rtTA	This study	Addgene #233202
pAAV-CMV-LNI-bGH	This study	Addgene #233203
pAAV-CAG-SNAP-p53DD-IRES-HRAS(G12V)-bGH	This study	Addgene #233204
pFUW-LNI	This study	Addgene #233205
pFUW-SNAP-p53DD-IRES-HRAS(G12V)	This study	Addgene #233206
pMXs-jRCaMP1b	This study	Addgene #233207
Software and algorithms		
Code	This study	https://doi.org/10.5281/zenodo.14851664
Adobe Illustrator CC	Adobe Systems	https://www.adobe.com
Python 3	N/A	https://www.python.org
ImageJ	N/A	https://imagej.net
FlowJo	N/A	https://www.flowjo.com
Cell Ranger v6.1.1	10x Genomics	https://www.10xgenomics.com
R 3.4.1 R Project	N/A	https://www.r-project.org
MATLAB	MathWorks	https://www.mathworks.com
Other		
AAV2 packaging service	VectorBuilder	https://en.vectorbuilder.com

EXPERIMENTAL MODEL AND STUDY PARTICIPANT DETAILS

Cell lines and tissue culture

HEK293T, Plat-E, and mouse embryonic fibroblasts were cultured in DMEM supplemented with 10% FBS at 37°C, 5% CO_2. Plat-E cells were selected using 10 μg/mL blastocidin and 1 μg/mL puromycin every three passages. Cultures were periodically tested for mycoplasma.

MEF dissection and isolation

C57BL/6 mice were mated with mice bearing the Hb9::GFP reporter. Mouse embryonic fibroblasts were isolated at E12.5-E14.5 under a dissection microscope. Embryos were sorted into non-transgenic and Hb9::GFP+ by using a blue laser to illuminate the spinal cord to identify the presence of Hb9::GFP+ cells. After removing the head and internal organs to avoid contaminating neurons and other cells, razors were used to break up the tissue for 5 minutes in the presence of 0.25% Trypsin-EDTA. Up to two embryos were processed at the same time. The preliminary suspension was neutralized, resuspended, and triturated with 0.25% Trypsin-EDTA. Again, the suspension was neutralized, resuspended, and filtered through a 40 μm cell strainer. MEF cultures were expanded on 0.1% gelatin coated 10 cm dishes, using one 10 cm dish per embryo. MEFs were expanded until ~80% confluent, passaged, and expanded for at least 3-4 days. Passage 1 MEFs were tested for mycoplasma, cryopreserved in 90% FBS and 10% DMSO, and kept in liquid nitrogen.

Animals

All *in vivo* experiments involving the use of mice were conducted according to a protocol approved by the Boston University IACUC (Protocol Number: PROTO202000045). Female C57BL/6 mice (RRID:IMSR_JAX:000664) were used for all *in vivo* experiments and underwent surgical procedures at 8 weeks of age. All experiments involving mice were conducted within approved Boston university facilities and mice were housed in a 12-hour light/dark cycle in a for-purpose facility with controlled temperature and humidity. Mice were provided with food and water ad libitum. Mice were administered post-surgical analgesia (buprenorphine, 0.1mg/kg) for 2 days after each surgery. No animals in the study that received cell grafts were administered with any immunosuppression drugs.

METHOD DETAILS

Plasmid construction

Entry vectors were constructed by Gibson and Golden gate cloning. Viral vectors were constructed by Gateway cloning into pMXs-WPRE-DEST, pFUW, or pAAV-DEST using an LR reaction for retro, lenti, or AAV, respectively. Viral plasmids were confirmed via Sanger or whole plasmid sequencing. For a complete list of plasmids, see Table S1.

Please cite this article in press as: Wang et al., Compact transcription factor cassettes generate functional, engraftable motor neurons by direct conversion, Cell Systems (2025), https://doi.org/10.1016/j.cels.2025.101206

Viral transduction and iMN conversion of MEFs

Plat-E cells were seeded at 850k per 6-well onto 6-well plates coated with 0.1% gelatin for at least 10 minutes at room temperature. The next day, ~80% confluent Plat-E cells were transfected with 1.8 μg of DNA per well using a 4-5:1 ratio of μg PEI:μg DNA. The next day, a media change was performed with 1.25 mL fresh DMEM supplemented with 10% FBS and 25 mM HEPES to help buffer. MEFs were also seeded at 10k per 96-well onto 96-well plates coated with 0.1% gelatin. The next day, viral supernatant was collected, filtered through a 0.45 μm filter, and 1.25 mL fresh DMEM supplemented with 10% FBS and 25 mM HEPES was added again to the Plat-E cells. MEFs were transduced with 11 μL of viral supernatant per viral cassette. Fresh DMEM supplemented with 10% FBS was added to reach a final volume of 100 μL per 96-well. 5 μg/mL polybrene was supplemented to increase transduction efficiency. Transduction was repeated for a second day. One day after the second viral transduction was considered 1 dpi and 100 μL per 96-well fresh media was swapped in. At 3 dpi, media was switched to N3 media (DMEM/F-12 supplemented with N2, B27, and neurotrophic growth factors, BDNF, CNTF, GDNF, FGF all at 10 ng/mL).[51,92] For conditions with RepSox, 7.5 μM RepSox was also supplemented into the N3 media starting at 3 dpi. For experiments needing larger well sizes, MEF seeding and viral supernatant volumes were scaled accordingly by well surface area.

Quantification of conversion yield and purity

Converted cells were dissociated using 0.025% Trypsin-EDTA prior to 6 dpi and DNase/papain from 6 dpi onwards. One vial of papain (>100 U/vial) and one vial DNase (>1,000 U/vial) were dissolved in 6 mL of DMEM/F-12. 50 μL of this dissociation media was used per 96-well. Cells were incubated with dissociation media at 37°C, 5% CO_2 for ~15 minutes or until starting to detach. 100 μL of media was added to neutralize the reaction, then cells were resuspended in 300 μL PBS. All cells in a well were recorded using flow cytometry to detect Hb9::GFP fluorescence. iMNs were defined by gating the brightest Hb9::GFP fluorescent cells.[51] (Normalized) Yield was calculated by dividing the total number of Hb9::GFP positive cells detected via flow by the total number of initially seeded cells which was generally 10k/96-well. Purity was calculated by dividing the total number of Hb9::GFP positive cells by the total number of cells detected via flow. Total yield was measured as the total number of Hb9::GFP positive cells detected via flow.

$$\text{(Normalized) Yield (\%)} = \frac{\#\ \text{Hb9::GFP positive cells}}{\#\ \text{initial seeded cells}} \times 100\%$$

$$\text{Purity (\%)} = \frac{\#\ \text{Hb9::GFP positive cells}}{\#\ \text{total cells detected}} \times 100\%$$

$$\text{Total Yield (\#)} = \#\ \text{Hb9::GFP positive cells}$$

CellTrace labeling to measure cellular proliferation

At 1 dpi, cells were first washed with PBS. Then 100 μL/96-well of 1μM CellTrace-Far Red or 5μM CellTrace-Violet in PBS was added. Cells were incubated at 37°C, 5% CO_2 for 30 minutes. Then the staining solution was removed, cells were washed with media to remove residual stain, then fresh media was added. Cells were then cultured or converted as normal. CellTrace fluorescence was detected by flow cytometry. Cells that undergo a period of hyperproliferation were identified by dilution of CellTrace dye over 72 hours from 1 to 4 dpi for MEF conversion and over 144 hours from 1 to 7 dpi for human conversion. We denote cells with a history of rapid proliferation at the time point assayed as hyperproliferative (hyperP) and all other cells at 4 dpi as non-hyperP relative to the CellTrace dilution in a control puro infection condition to account for effects on proliferation induced by viral transduction. For MEF and human conversion, hyperP cells are defined relative to the 20%-lowest and 5%-lowest fluorescent cells, respectively, in a control puro infection condition for a given biological replicate.

Flow cytometry and FACS

An Attune NxT Acoustic Focusing Cytometer was used for flow cytometry analyzer experiments. A 405 nm laser with a 440/50 filter was used for blue fluorescence (DAPI, CellTrace-Violet), a 488 nm laser with 510/10 filter was used for green fluorescence (GFP), a 561 nm laser was used with 585/16 filter for red fluorescence (Alexa Fluor 594, mRuby2), and a 638 nm laser with a 670/14 filter was used for far red fluorescence (Alexa Fluor 647, CellTrace-Far Red, Zombie NIR). FSC-A and SSC-A were used to gate cells, while FSC-H and FSC-A were used to gate singlets using FlowJo. Singlets were exported as csv files to analyze using Python.

FACS was performed using a BD FACSAria. A 488 nm laser with 530/30 filter was used for green fluorescence (GFP), a 561 nm laser with 610/20 filter was used for red fluorescence (jRCaMP1b) and a 640 nm laser with a 670/30 filter was used for far red fluorescence (CellTrace-Far Red, Zombie NIR, Snap-Cell 647-SIR). Cells were sorted into N3 media supplemented with penicillin-streptomycin. For replating experiments, cells were resuspended in their appropriate medias, counted, and replated at 10k/96-well. Penicillin and streptomycin were included for the rest of conversion after sorting.

For all cytometry experiments, appropriate controls were included to assess negative populations (*e.g.* un-stained cells, single color controls, secondary antibody only controls, non-targeting antibody controls, etc.).

Fixation and immunofluorescent staining

For plate imaging, cells were fixed with 3.7% paraformaldehyde for 1 hour at 4°C. Cells were washed three time with cold PBS and permeabilized with 0.5% Tween/PBS overnight at 4°C. Cells were then blocked with 5% FBS and 0.1% Tween/PBS for 1 hour at 4°C. Cells were then incubated with primary antibody diluted in blocking solution (5% FBS and 0.1% Tween/PBS) overnight at 4°C. Cells were then washed three times with cold 0.1% Tween/PBS, with the third wash being left for at least 20 minutes. Cells were then incubated with secondary antibody diluted in blocking solution (5% FBS and 0.1% Tween/PBS) for 1 hour at 4°C. Cells were then washed three times with cold 0.1% Tween/PBS and 0.1 μg/mL DAPI staining was added for 10 minutes. Cells were washed three more times with cold 0.1% Tween/PBS and imaged. In between incubation steps, the plate was kept covered in foil.

For flow cytometry, cells were dissociated and fixed with 3.7% paraformaldehyde for 15 minutes at room temperature. Cells were permeabilized by 200 μL of 0.5% Tween/PBS for 15 minutes at room temperature, and washed with PBS. 200 μL of primary antibody diluted in blocking solution (5% FBS and 0.1% Tween/PBS) was added and incubated at 4°C for 2 hours or overnight with rotation for mixing. Cells were washed three times with 1 mL cold 0.1% Tween/PBS, with the third wash being left for at least 30 minutes at 4°C. Cells were then incubated with 800 μL of secondary antibody diluted in blocking solution for 30 minutes at 4°C and washed three times with 1 mL cold 0.1% Tween/PBS. In between incubation steps, cells were kept covered in foil. The primary antibodies used in this study were: rabbit anti-Ki67 (1:100, GeneTex, GTX1667, RRID:AB_422351); mouse anti-Ngn2 (1:500, Santa Cruz, sc-293430); mouse anti-Isl1 (2 μg/mL, DHSB, 40.2D6, RRID:AB_528315); mouse anti-Lhx3 (2 μg/mL, DHSB, 67.4E12, RRID:AB_2135805); mouse anti-Hemagglutinin (HA) (1:1,000, Biolegend, 901501, RRID:AB_2565006); mouse anti-TUBB3 (1:500, Biolegend, 801202, RRID:AB_10063408); rabbit anti-MAP2 (1:500, Cell Signaling Technology, #4542, RRID:AB_10693782); goat anti-Choline Acetyltransferase (ChAT) (1:500, MilliporeSigma, AB144P, RRID:AB_2079751). The secondary antibodies used in this study were: donkey anti-mouse Alexa Fluor 647 (1:500, Invitrogen, A-31571, RRID: AB_162542); donkey anti-rabbit Alexa Fluor 594 (1:500, Invitrogen, A-21207, RRID: AB_141637); donkey anti-rabbit Alexa Fluor 647 (1:500, Invitrogen, A-31573, RRID:AB_2536183); goat anti-mouse Alexa Fluor 488 (1:500, Jackson ImmunoResearch Labs, 115-546-146, RRID:AB_2338868); donkey anti-goat Alexa Fluor 647 (1:500, Jackson ImmunoResearch Labs, 705-605-147, RRID:AB_2340437).

Western blot assay

Cells were lysed at 4 dpi using RIPA buffer with 1 mM PMSF. Cells were sheared with blunt 21-gauge needles, and the lysate was clarified by centrifugation at 14,000xg at 4°C. Protein concentration was measured using a Bradford assay. Samples were separated using electrophoresis in a 12.5% bis-tris gel, with 20 ug of total cell protein loaded per well. The protein was transferred to a PVDF membrane using the iBlot 2 dry blotting system. Blots were incubated with primary antibodies overnight at 4°C and for 1 hour at room temperature with secondary antibodies. HRP was detected using SuperSignal West Femto Maximum Sensitivity Substrate, and blots were imaged using the ChemiDoc MP Imaging System. The primary antibodies used in this study were: mouse anti-β-Actin (8H10D10) (1:50k, Cell Signaling Technology, #3700, RRID:AB_2242334); rabbit anti-Ras (G12V Mutant Specific) (D2H12) (1:1000, Cell Signaling Technology, #14412, RRID:AB_2714031); rabbit anti-p53 (D2H9O) (1:20k, Cell Signaling Technology, #32532, RRID:AB_2757821). The secondary antibodies used in the study were: goat anti-mouse IgG H&L (HRP) (1:50k, Abcam, ab205719, RRID:AB_2755049); goat anti-rabbit IgG H&L (HRP) (1:50k, Abcam, ab6721, RRID:AB_955447).

AAV transduction

Single-stranded adeno-associated virus (AAV) was manufactured with research grade AAV packaging from VectorBuilder with serotype 2 and stored at -80°C. To determine MOI, frozen AAV was resuspended in DMEM with 10% FBS to reach a final volume of 200 μL per 96-well. MEFs were seeded at a lower 2.5k/96-well density onto a 0.1% gelatin-coated plate, and transduced with 1:2 serial dilutions of AAV-CAG-GFP-WPRE. 5 μg/mL polybrene was supplemented for similarity with retroviral transduction. Cells with viral media were then centrifuged at 1,500xg for 30 minutes at 32°C to further increase transduction efficiency via spinfection. Fresh media was changed the following day. GFP expression was measured at 4 dpi. The percent of GFP-positive MEFs at 4 dpi vs. virus volume was plotted and fit to a Poisson distribution to determine the number of transducing units (TU) per genome copy (GC). It was determined that 1 TU was equivalent to $\sim 2.2 \times 10^6$ GC. For AAV-CMV-LNI-bGH (10.7×10^{11} GC/mL) and AAV-CAG-SNAPp53DD-IRES-HRAS^{G12V}-bGH (2.3×10^{11} GC/mL) that meant 25 μL and 118 μL for 2.5k MEFs to reach MOI=5.

Morphology quantification of Hb9::GFP-positive cells

All Hb9::GFP-positive cells found were imaged for each condition per biological replicate. Hb9::GFP-positive cells with neuronal morphology were classified as having a tight soma with neurites. Annotation was performed manually using ImageJ.

Lentiviral transduction and doxycycline induction

HEK293Ts were seeded at 6.5 million per 10 cm dish onto 10 cm dishes coated with 0.1% gelatin. The next day, each dish of 293Ts was transfected with 10.8 ug pLK-packaging plasmid, 1.2 ug of pHDMG envelope plasmid, and 12 ug of transfer lenti-TRE3G plasmid using a 4-5:1 ratio of ug PEI:μg DNA. 6-8 hours later, a media change was performed with 6.5 mL of 25 mM HEPES buffered DMEM with 10% FBS. 24, 48, and 72 hours later, viral supernatant was collected and stored at 4°C and was replaced with fresh media after

the first two collections. After the third collection, the viral supernatant was filtered with a 0.45 μM filter and was mixed with 1 volume Lenti-X concentrator to 3 volumes viral supernatant and incubated at 4°C for 1-3 days. Next, the virus was pelleted by centrifugation at 1,500 x g for 45 minutes at 4°C. The supernatant was removed, and the pellets were resuspended in HDF media to a final volume of 200 μL per 10 cm dish, and stored at -80°C until use.

MEFs were seeded at 10k/96-well in 0.1% gelatin-coated plates. Frozen lentivirus was mixed with fresh 11 μL viral supernatant of pMXs-rtTA-WPRE produced by Plat-E cells as described above, and resuspended to a final total volume of 100 μL/96-well. 5 ug/mL polybrene was supplemented and plates were centrifuged at 1,500 x g for 30 minutes at 32°C to further increase transduction efficiency via spinfection. The following day, fresh media was replaced. 1 μg/mL doxycycline was supplemented beginning at 1 dpi to induce transcription from TRE3G and rtTA.

At 14 dpi, cells were also stained for SNAPp53DD. N3 media supplemented with 0.3 μM Snap-Cell 647-SIR was incubated with cells for 30 min at 37°C, 5% CO_2. After, cells were washed with N3 and incubated for another 30 min at 37°C, 5% CO_2 in fresh N3 media. Hb9::GFP-positive and SNAPp53DD-positive cells were sorted by FACS and recovered in N3 with RepSox and penicillin-streptomycin and no doxycycline. Half media changes were then performed every other day for 14 days.

Seeding titration transduction

Plat-E cells were seeded and transfected as described above. The initial HEPES-buffered, viral supernatant was collected and 1.25 mL fresh DMEM supplemented with 10% FBS and 25 mM HEPES was added again to the Plat-E cells. The additional viral supernatant was collected the following day, mixed with the previous, and the total ~2.5 mL viral supernatant was filtered through a 0.45 μm filter.

MEFs were seeded at 10k/96-well and 1:2 serially diluted for 5k, 2.5k, and 1.25k/96-well. The following day, 10k/96-well seeded MEFs were transduced with 11 μL of viral supernatant per viral cassette and viral supernatant was 1:2 serially diluted to 5.5, 2.75, 1.375 μL viral supernatant/96-well to keep MOI constant. Transductions were done with 5 μg/mL polybrene and plates were centrifuged at 1,500 x g for 30 minutes at 32°C to further increase transduction efficiency via spinfection. Fresh media was changed the next day and cells were converted as normal.

jRCaMP1b timelapse

Cells were converted using Plat-E produced retroviruses as described. jRCaMP1b was delivered by retrovirus as well. At 14 dpi, cells were sorted by FACS for Hb9::GFP and jRCaMP1b. Sorted cells were replated at 40k/96-well. Glass-bottom 96-well plates were coated with 0.1% gelatin for at least 10 minutes at room temperature. Then a secondary coat of 5 μg/mL CellAdhere Laminin-521 in PBS (with Calcium, Magnesium) was added by incubation for at least 2 hours at 37°C. Cells were replated in appropriate media (N3 with BDNF, CNTF, GDNF, FGF and RepSox; or N3 without BDNF, CNTF, GDNF, FGF) with penicillin-streptomycin. Half media changes were performed every other day. At 7 days post-sort, cells were imaged at 37°C for 5 minutes at ~6.3 frames per second using the Nikon Ti2-E perfect focusing system.

Timelapse images were processed using a built-in Nikon Ti2-E ND processing tool to equalize intensity in time. Traces of fluorescence over time were obtained by manually drawn regions of interest (ROI) using ImageJ. Traces of normalized jRCaMP1b fluorescence ($\Delta F/F_o$) over time was calculated as $(F- F_o)/F_o$ where F is the fluorescence over time and F_o is the minimum fluorescence detected for that ROI. A control ROI containing a cell with no spontaneous spiking is shown for each to show non-signaling jRCaMP1b fluorescence over time is stable after intensity equalization. Timelapse videos were edited in MATLAB solely to emphasize Ca^{2+} spikes for visualization. Briefly, ΔF multiplied by 5 was adding to F for each time point. All ROI traces in the manuscript represent only the intensity equalized traces without further processing.

Electrophysiology measurements using multi-electrode array (MEA)

Cells were converted and sorted for Hb9::GFP by FACS at 14 dpi. Cells were then replated onto the MaxOne High-Density Microelectrode Array (HD-MEA) System. The MEA chips were prepared according to manufacturer's instructions. Briefly, a 1% Tergazyme solution was used to clean chips. A primary coating was done by incubation with 0.7% polyethyleneimine (PEI) in borate buffer solution for 1 hour at 37°C. Then a secondary coating was added by incubation with 0.2 mg/mL laminin in N3 media for 1 hour at 37°C. Then 50 μL of 2,000 cells/μL solution was added to center of each chip for a total of 125k cells/chip. Cells were incubated for 1 hour at 37°C, 5% CO_2. Then 600 μL of appropriate media (N3 with BDNF, CNTF, GDNF, FGF and RepSox; or N3 without BDNF, CNTF, GDNF, FGF) with penicillin-streptomycin was added. Primary rat cortical neurons were also plated at the same density and cultured with N3 (with BDNF, CNTF, GDNF, FGF) and RepSox. Half media changes were performed every other day. Measurements were taken at least 2 weeks after replating to allow cells to recover. 16 hours before taking measurements, media was changed to BrainPhys Neuronal Medium with penicillin-streptomycin to encourage spontaneous firing.

Single cell RNA-sequencing

For scRNA-seq libraries generated for this work, cells were converted as described. Prior to loading onto 10X, cells were sorted via FACS with 1:1000 Zombie NIR spiked in prior to flow to sort for live cells. For the 4 dpi sample, a CellTrace-Far Red stain was also included starting at 1 dpi to sort for hyperproliferative cells. For 14 dpi samples, converted iMNs were also sorted via FACS for Hb9::GFP positive cells. Prior to loading, cells were resuspended, counted, confirmed for >90% viability by trypan blue staining, and loaded for a target recovery of ~1,500 cells per condition. Libraries were generated using a 10X Chromium Next GEM Single

Cell 3' kit v3.1 (dual index) following manufacturers protocols using 12 cycles of amplification in cDNA generation. RT-PCR and Advanced Analytical Technologies Inc fragment analyzers were used to confirm pooled library quality. NovaSeq S4 kit was used to sequence pooled libraries with 150 reads for the cell barcode + UMI, 8 cycles for the i7 and i5 sample indices, and 150 cycles for the insert. Sequenced libraries were aligned to a custom reference based on GRCm39 with the eGFP marker gene added using CellRanger (v6.1.1). ~30-60k reads/cell were generated with the exception of LNI + DDRR converted cells at 4 dpi which had ~5k reads/cell.

Single cell RNA-seq analysis

Cluster analysis via Seurat

Cells were filtered for < 8% mitochondrial reads, and between 200 and 10,000 features. The SCTransform function was used to normalize libraries. An elbow plot was used to determine the number of PCA's to use for clustering. Seurat's FindNeighbors and FindClusters functions were used to cluster cells and the resolution was adjusted such that clusters largely belonged to conversion conditions. EmbMNs collected at E12.5 were clustered independently to identify median motor column (MMC) motor neurons. An MMC cluster was isolated using marker genes, Mnx1, Isl1, Lhx3, and GFP.[78,94–97] For simplicity of notation, we denoted these simply "EmbMN" and ignored all non-MMC embMNs for analysis. After incomplete motor neurons were identified, this cluster was removed for further analysis.

Surgery procedures for *in vivo* cell grafts

Surgery procedures

All procedures were performed on mice under general anesthesia achieved through inhalation of isoflurane (1.5-3%) in oxygen-enriched air that was administered via a mouse anesthesia mask that was attached to a stereotactic device. Prior to surgery the head of the mouse was shaved and sterilely prepared with betadine and alcohol scrubs. All surgery procedures were conducted with the mouse stably positioned within a stereotactic frame using a mouse snout clamp, tooth bar, and dual sided ear bars. A heating pad positioned under the mouse was used to ensure maintenance of body temperature.

Craniotomy procedure

A single midline skin incision made using a scalpel was used to expose the dorsal surface of mouse skull and the surface of the skull is cleaned dry with a sterile cotton swab. Using a high-speed surgical drill, a small craniotomy was made over the left coronal suture that was visually aided by a stereomicroscope. As small rectangular flap of bone encompassing sections of the frontal and parietal bone was removed to expose the brain in preparation for injection. Saline was applied to keep the exposed brain tissue moisten throughout injection procedures.

Stroke lesion model

To create small focal ischemic strokes, 0.5 μL of L-NIO (N5-(1-Iminoethyl)-L-ornithine) (Cat. No. 400600-20MG, Millipore Sigma) (27.4 mg/ml (130 μM) in sterile PBS), an inhibitor of endothelial nitric oxide synthase, was injected into the caudate putamen nucleus at 0.2 μL/min using target coordinates relative to Bregma: +1.0 mm A/P, +2.5 mm L/M and −3.0 mm D/V using pulled borosilicate glass micropipettes (WPI, Sarasota, FL, #1B100-4). Glass micropipettes were mounted to the stereotaxic frame via specialized connectors and attached, via high-pressure polyetheretherketone (PEEK) tubing, to a 10 μL syringe (Hamilton, Reno, NV, #801 RN) controlled by an automated syringe pump (Pump 11 Elite, Harvard Apparatus, Holliston, MA). After the full volume of L-NIO solution had been injected, the pipette was allowed to rest at the injection site for 4 minutes before being slowly removed from the brain over the course of 1 minute. Following L-NIO injection, the surgical incision site was sutured and the animals were allowed to recover for 48 hours before undergoing iMN graft injections via a second surgery as described below.

iMN graft injections

iMN grafts were made in healthy mouse brain (n=5) and L-NIO stroke injured brain (n=5) at 48 hours after L-NIO injection. Healthy mice received a craniotomy prior to cell injections whereas the already created cranial window in stroke injured mice was not modified prior to cell injection. Two million imN cells recovered by FACS for Hb9::GFP-positive cells were resuspended in 70μL of basal media (N3, neurotrophic factors, RepSox, and penicillin-streptomycin) to create a concentrated cell solution at 28.6K cells/μL. The concentrated cell solution was backloaded into a pulled glass micropipette prior to connecting to the stereotaxic frame. The one cell stock was injected into all animals with injections alternating between mice from the healthy and stroke groups. 1 μL of cell solution was injected into the same striatal regions as that used to create the stroke at 0.15 μL/min using target coordinates relative to Bregma: +1 mm A/P, +2.5 mm L/M. The pipette was lowered to −3.5 mm D/V for the start of the injection and moved up +0.5mm twice over the course of the injection to a final location of −2.5 mm D/V to improve deposition of cells in brain tissue. The micropipette was allowed to dwell in the brain at the injection site for an additional 4 minutes at the end of the injection. The micropipette was then removed from the brain slowly and incrementally over a 1-minute period.

Immunohistochemistry for *in vivo* cell grafts

Transcardial perfusions

After terminal anesthesia by overdose isoflurane inhalation, mice were perfused transcardially with heparinized saline and 4% paraformaldehyde (PFA) that was prepared from 32% PFA Aqueous Solution (Cat# 15714, EMS), using a peristaltic pump at a rate of 7 mL/min. Approximately, 10 mL of heparinized saline and 50 mL of 4% PFA was used per animal. Brains were immediately dissected after perfusion and post-fixed in 4% PFA for 6 hours at room temperature. After PFA post-fixing, brains were cryoprotected in 30%

sucrose in Tris-Buffered Saline (TBS) at 4°C for at least 3 days with the sucrose solution replaced once after 2 days and stored at 4°C until further use.

Immunohistochemistry

Coronal sections of mouse brains receiving grafts were cut (40 μm thick) using a Leica CM1950 Cryostat. Tissue sections were stored in TBS buffer at 4°C in individual wells of a 96 well, plate prior to staining. Tissue sections were processed for immunofluorescence using free floating staining protocols described in comprehensive detail previously using donkey serum to block and triton X-100 to permeabilize tissue.[37,78] The primary antibodies used in this study were: rabbit anti-Hemagglutinin (HA) (1:1000, Sigma #H6908, RRID:AB_260070); goat anti-HA (1:800, Novus, NB600-362, RRID:AB_10124937); rat anti-Gfap (1:1000, Thermofisher, #13-0300, RRID:AB_86543); guinea pig anti-NeuN (1:1000, Synaptic Systems, 266 004, RRID:AB_2619988); rabbit anti-Neurofilament M (145kDa) (NFM) (1:500, Millipore Sigma, AB1987, RRID:AB_91201), chicken anti-GFP (1:2000, Abcam, ab13970, RRID:AB_300798), rabbit anti-GFP (1:500, Abcam, ab290, RRID:AB_303395), goat anti-Choline Acetyltransferase (ChAT) (1:500, MilliporeSigma, AB144P, RRID:AB_2079751) and rabbit anti-DARPP-32 (19A3) (1:400, Cell Signaling, 2306, RRID:AB_823479). All secondary antibodies used in this study were purchased from Jackson ImmunoResearch (West Grove, PA). All secondary antibodies were affinity purified whole IgG(H+L) antibodies with donkey host and target species dictated by the specific primary antibody used. All secondary antibodies were stored in 50% glycerol solution and diluted at a concentration of 1:250 in 5% normal donkey serum in TBS when incubated with brain histological sections. Nuclei were stained with 4',6'-diamidino-2-phenylindole dihydrochloride (DAPI; 2ng/ml; Molecular Probes). Sections were mounted using ProLong Gold anti-fade reagent (ThermoFisher). Sections were examined and imaged using epifluorescence and deconvolution epifluorescence microscopy on an Olympus IX83 microscope. Orthogonal (3D) images were prepared using Zen 3.1 (Blue Edition) (Zeiss).

Quantification of immunohistochemistry

Quantification of immunohistochemistry staining intensity quantification was performed on whole brain section images taken with the 10X objective on the Olympus IX83 microscope. All images used for each comparable analysis were taken at a standardized exposure time and used the raw/uncorrected intensity setting. Quantification of antibody staining intensity was generated in the form of radial intensity profiles derived using NIH Image J (1.51) software and the radial profile angle plugin as detailed previously.[37,78] Total values for IHC stainings were determined by taking the integral (area under the curve) of the radial intensity profile.

Cell coverslips

iMNs purified via FACS for Hb9::GFP positive cells were cultured on 10 mm round coverslips (Thorlabs) coated with 0.1% gelatin in individual wells of a 24 well plate for 7 days following an initial seeding of 100,000 cells per well. iMNs were fixed with 4%PFA for 30 minutes and coverslips were then stained using IHC methods and antibodies described above.

Fluorescent Imaging

Images not taken for immunohistochemistry were imaged using a Keyence All-in-one fluorescence microscope BZ-X800. Timelapse for jRCaMP1b was taken using a Nikon Ti2-E fluorescence microscope.

QUANTIFICATION AND STATISTICAL ANALYSIS

Quantification and statistical analysis were performed using Python, R, MATLAB, and ImageJ. Code available upon request.

Cell Systems, Volume *16*

Supplemental information

Compact transcription factor cassettes generate functional, engraftable motor neurons by direct conversion

Nathan B. Wang, Honour O. Adewumi, Brittany A. Lende-Dorn, Adam M. Beitz, Timothy M. O'Shea, and Kate E. Galloway

SUPPLEMENTARY FIGURES

Fig. S1 Expression of conversion factors varies across polycistronic cassettes

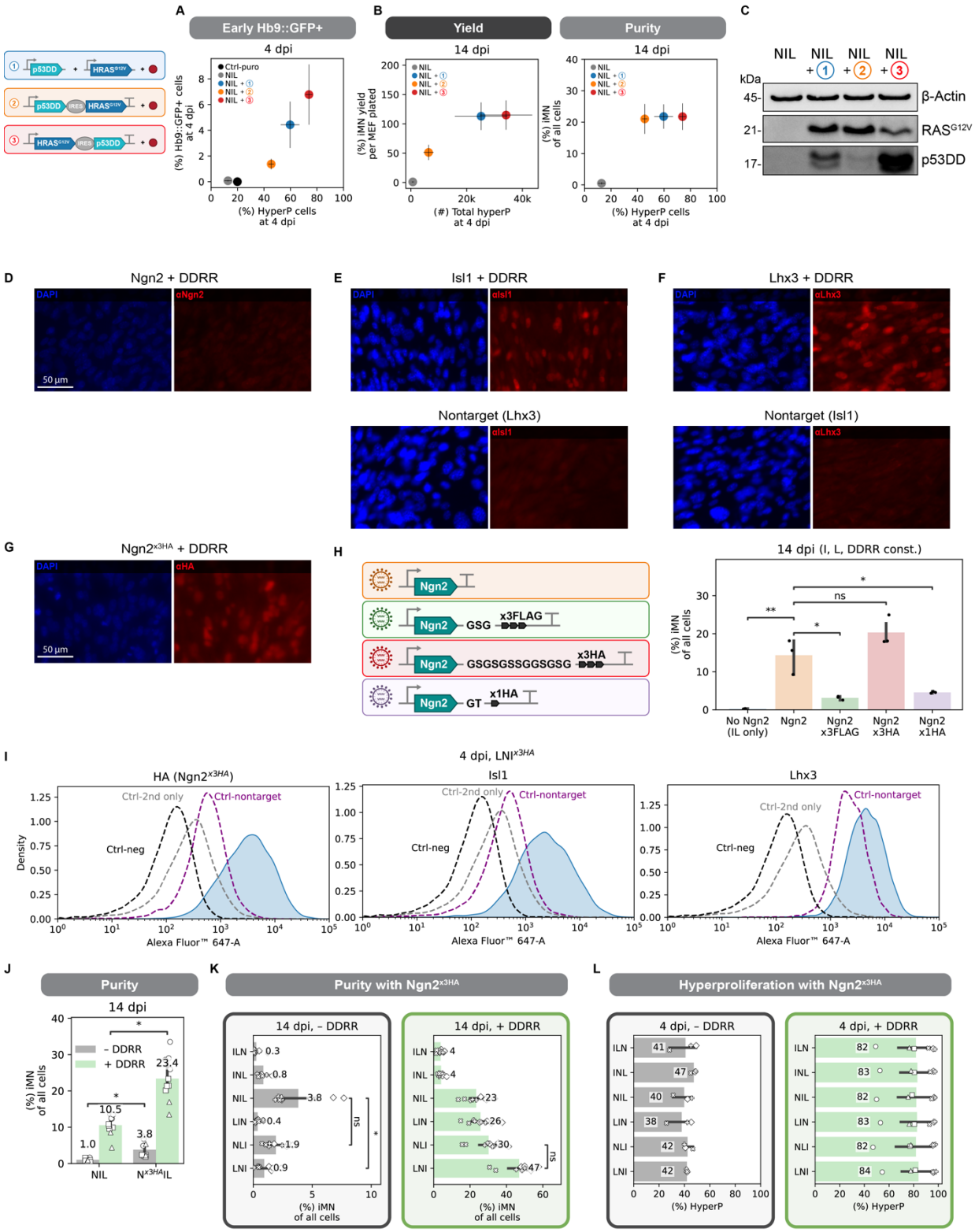

A-B. Hb9::GFP reporter activation vs. proliferation for different designs of the genetic portion of the DDRR cocktail (see Fig. 2D). (A) Hb9::GFP activation at 4 dpi vs hyperP percent at 4 dpi. (B) Conversion yield at 14 dpi vs. hyperP total number at 4 dpi (left) and conversion purity at 14 dpi vs. hyperP percent at 4 dpi (right). Mean is shown ± standard error of mean (SEM); n=4 biological replicates per condition.

C. Western blot for p53DD and RAS^{G12V} expression at 4 dpi with β-Actin for a loading control. Lysate was collected at 4 dpi from cells infected with NIL plus different designs of the genetic portion of the DDRR cocktail (see Fig. 2D): (1) NIL + DD + R, (2) NIL + DDIR, or (3) NIL + RIDD.

D-F. Images demonstrating Isl1 and Lhx3 antibodies properly localize to specific to expression of the transgene while Ngn2 fails. Nontargeting control for Isl1 antibody was Lhx3 + DDRR and nontargeting antibody for Lhx3 was Isl1 + DDRR. Scale bar represents 50 μm.

G. Image demonstrating HA staining properly localizes to the nucleus for cells infected with $Ngn2^{x3HA}$. Scale bar represents 50 μm.

H. Conversion yield at 14 dpi for Ngn2 with different linker-tags. Mean is shown with 95% confidence interval; two-tailed t-test with Bonferroni correction.

I. Histograms of immunofluorescence from staining for HA ($Ngn2^{x3HA}$), Isl1, and Lhx3 measured via flow cytometry. Control negative, secondary stain only, and a nontargeting control (cells infected with just +DDRR) are shown in black, grey, and purple dashed lines, respectively.

J. Conversion purity at 14 dpi for the polycistronic NIL cassette ± DDRR for the untagged Ngn2 and the tagged $Ngn2^{x3HA}$.

K. Conversion purity at 14 dpi for the different polycistronic TF cassettes without DDRR (left) and with +DDRR (right). All cassettes contain the tagged $Ngn2^{x3HA}$. Mean is shown with 95% confidence interval; markers denote biological replicates; n=3 biological replicates per condition; one-tailed t-test with Bonferroni correction.

L. Proliferation for the different polycistronic transcription factor cassettes without DDRR (left) and with +DDRR (right) at 4 dpi. HyperP cells are defined relative to the 20%-lowest fluorescent cells in a control puro (Ctrl-puro) infected condition for a given biological replicate. Mean is shown with 95% confidence interval; markers denote biological replicates.

Significance summary: $p > 0.05$ (ns); $*p \leq 0.05$; $**p \leq 0.01$; $***p \leq 0.001$; and $****p \leq 0.0001$

Fig. S2 Ordering of transcription factor cassette influences expression levels and conversion rates

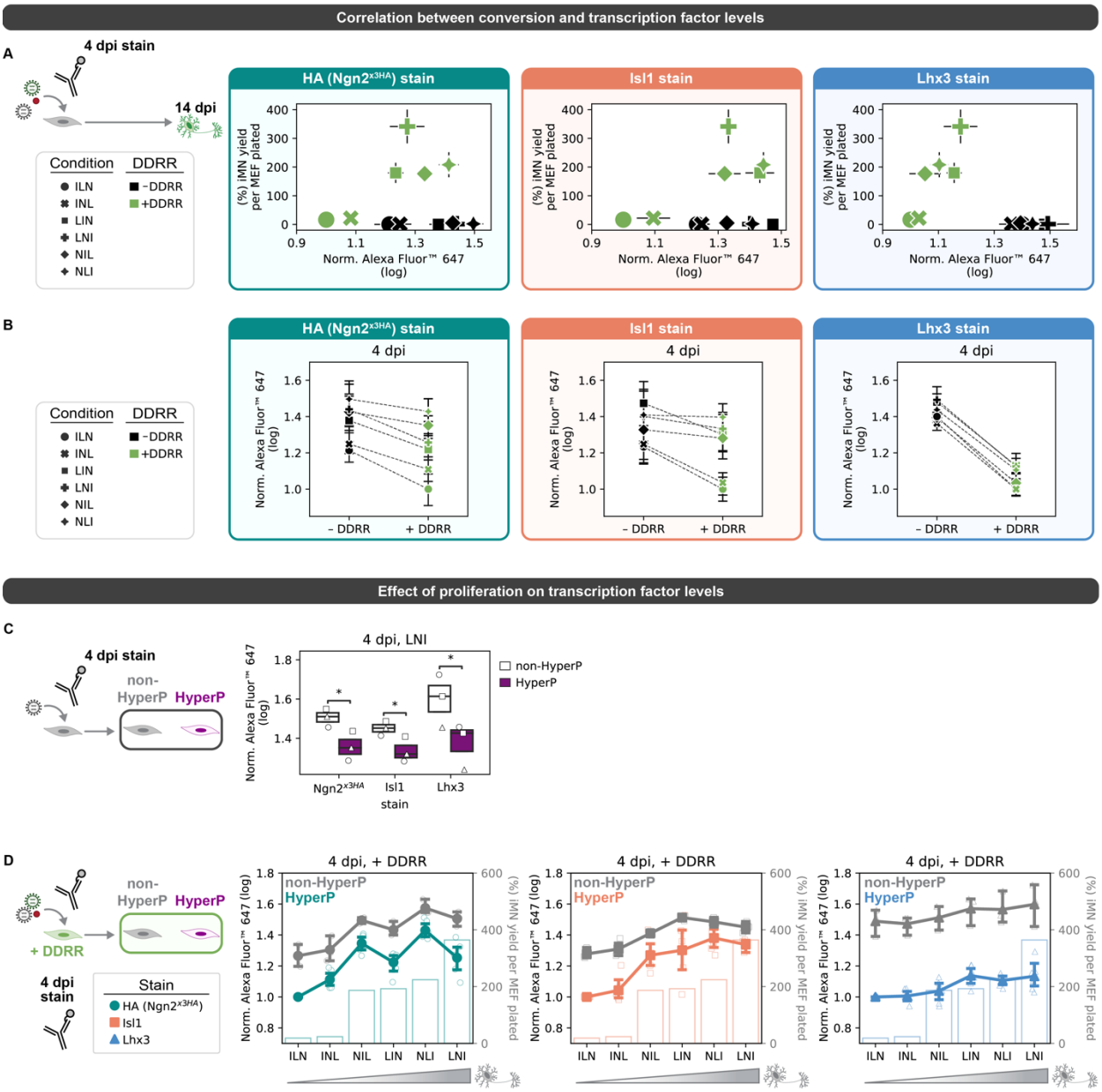

A. Conversion yield at 14 dpi vs. immunofluorescence at 4 dpi for the different polycistronic cassettes without DDRR (black) and with +DDRR (green). Mean is shown with ± standard error of mean (s.e.m.); n=3-6 biological replicates per condition; markers denote conversion cassette . Immunofluorescence is normalized such that the mean log expression for ILN + DDRR is 1 in each biological replicate.

B. Same immunofluorescence at 4 dpi as in Fig. S2A but a dashed line connects each polycistronic cassette without DDRR (black) and with +DDRR (green). Mean is shown with ± s.e.m.; n=3-6 biological replicates per condition; markers denote conversion cassette.

C. Transcription factor immunofluorescence at 4 dpi for HA/Ngn2^{x3HA} (left), Isl1 (middle), and Lhx3 (right) in non-hyperP vs. hyperP cells. Representative conversion condition shows cells converted with just LNI. Geometric mean is shown by markers with a boxplot; n=3 biological replicates per condition; markers denote biological replicates. Immunofluorescence is normalized such that the mean log expression for ILN + DDRR is 1 in each biological replicate.

D. Transcription factor immunofluorescence at 4 dpi for conversion with DDRR in non-hyperproliferative (grey) vs. hyperproliferative cells (colored) for HA/Ngn2^{x3HA} (left), Isl1 (middle), and Lhx3 (right). Polycistronic cassettes are ordered by increasing conversion events with DDRR (conversion yields with DDRR from Fig. 2H are overlaid as bar charts for reference). Mean with biological replicates are shown with ± s.e.m.; n=3-6 biological replicates per condition; marker and color denote antibody used.

Significance summary: p > 0.05 (ns) and *p ≤ 0.05

Fig. S3 Compact, single-transcript cassettes are portable to lenti and AAV for comparison of conversion

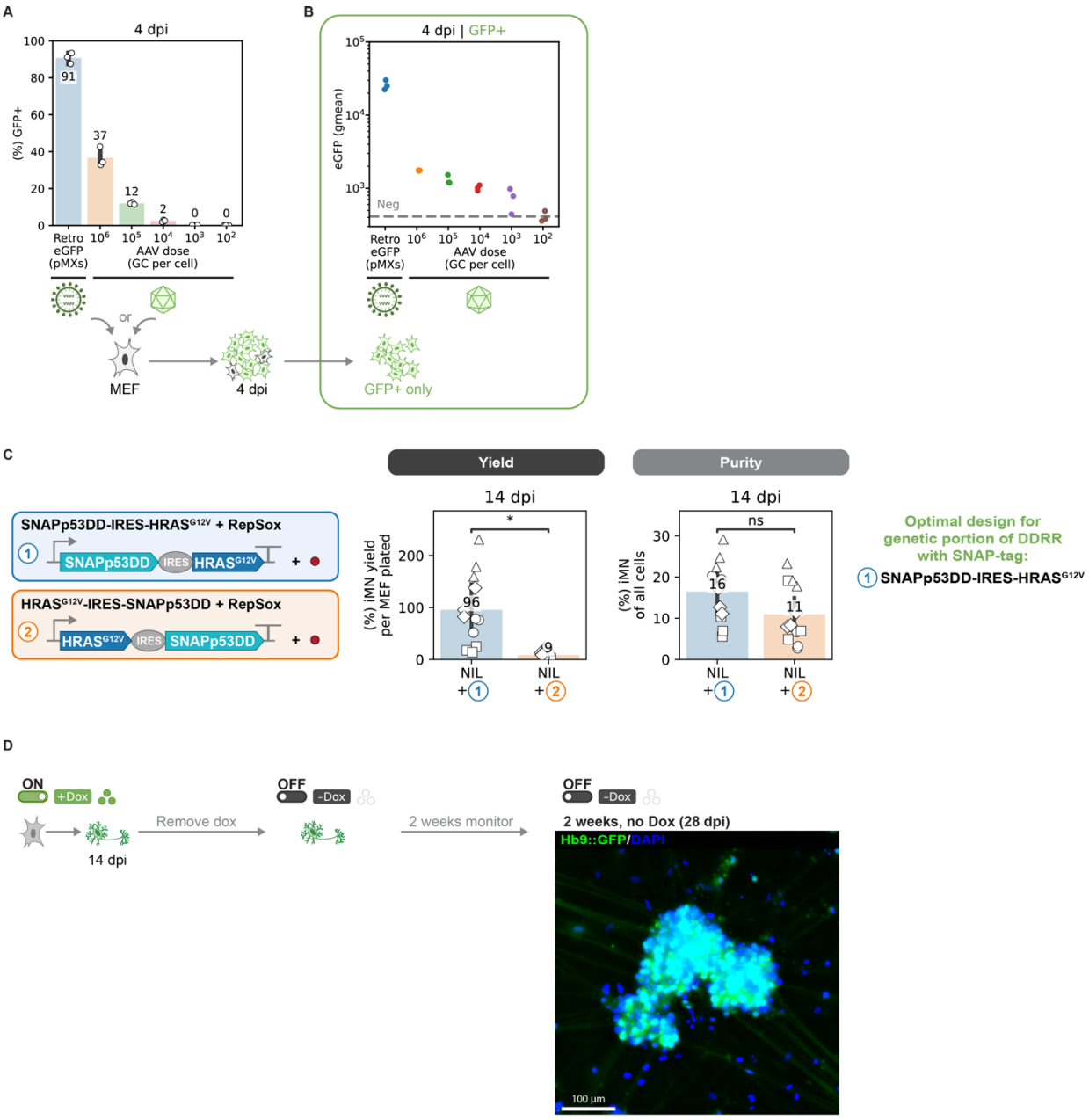

A-B. Titration of AAVs for transducing MEFs. An AAV expressing CAG-eGFP-WPRE was used to convert genome copies (GC) per cell to transducing units per cell by infecting MEFs with a range of 10^2 to 10^6 GC per cell seeded and detecting fluorescence by flow cytometry at 4 dpi. A control retrovirus (pMXs-eGFP-WPRE, on left/colored blue) was included to compare expression between an AAV and retrovirus in MEFs. The percent of GFP+ cells is shown in (B) and the GFP geometric mean (gmean) of the GFP+ cells is in (C). The dashed line indicates the GFP gmean of a negative control. n=1 biological replicate.

C. Conversion yield and purity (right) at 14 dpi for different designs (left) of the genetic portion of the DDRR cocktail. Design 1: SNAPp53DD-IRES-HRAS^{G12V}; Design 2: HRAS^{G12V}-IRES-SNAPp53DD. Mean is shown with 95% confidence interval; marker style denotes bio replicates; n=4 biological replicates per condition; two-tailed t-test.

D. Images of Hb9::GFP and DAPI as a nuclear stain of cells at 28 dpi converted by an inducible system (TRE3G-LNI + TRE3G-DDR + retro-rtTA) with dox for 14 days, followed by removal of dox for 14 days. Scale bar represents 100 µm.

Significance summary: $p > 0.05$ (ns); *$p \leq 0.05$; **$p \leq 0.01$; ***$p \leq 0.001$; and ****$p \leq 0.0001$

Fig. S4 Compact cassettes scale-up of conversion process to generate large numbers of neurons

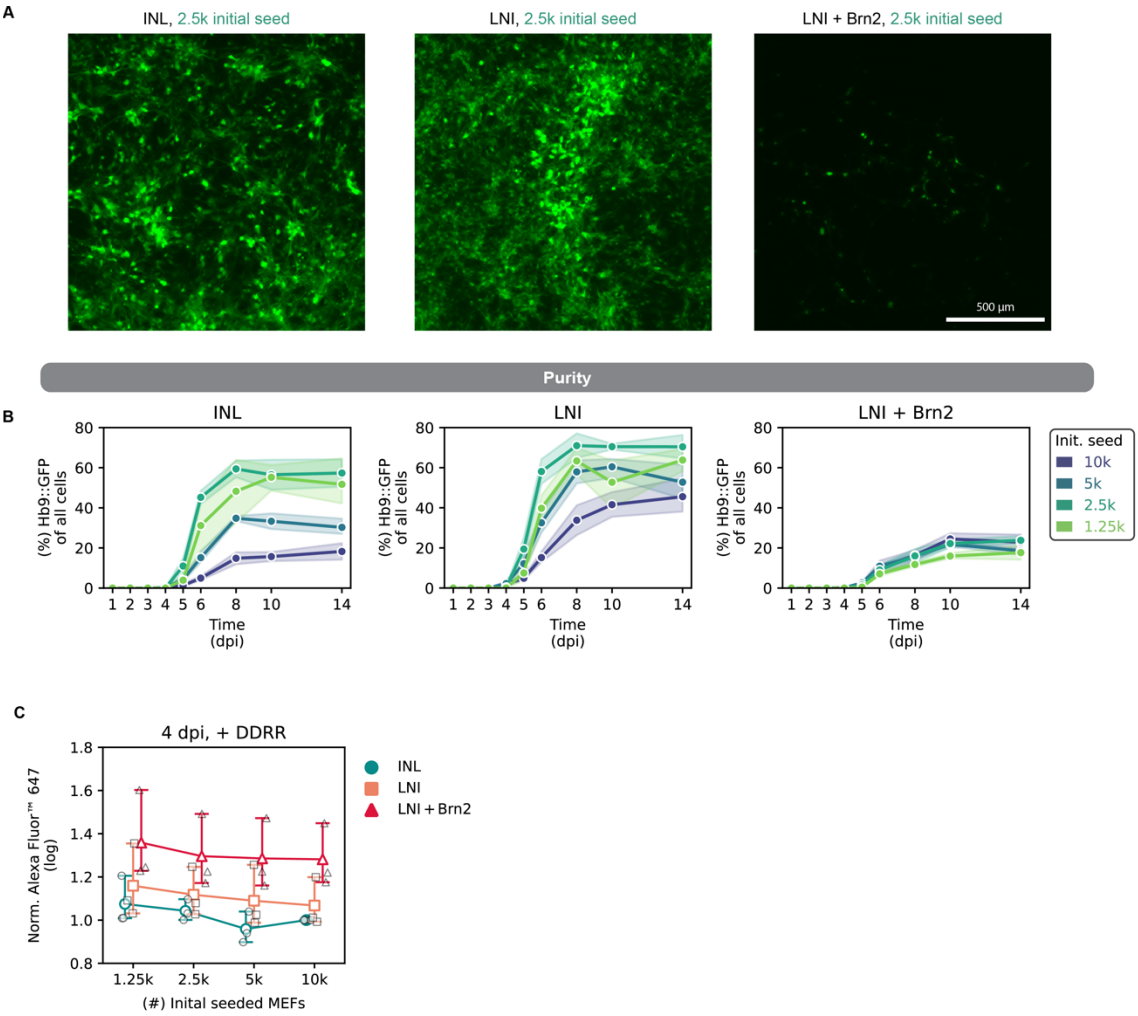

A. Hb9::GFP images of cells at 14 dpi converted by INL, LNI, or LNI + Brn2. All conditions were converted +DDRR with an initial seeding density of 2.5k MEFs per 96-well. Scale bar represents 500 µm.

B. Conversion purity as the percent of Hb9::GFP+ cells of all cells detected by flow from 1 to 14 dpi. All conditions were converted +DDRR. Mean is shown with 95% confidence interval; n=2 biological replicates per condition.

C. HA/Ngn2^{x3HA} immunofluorescence at 4 dpi for conversion with DDRR for different conversion TF cocktails across seeding densities (see Fig. 2B). Mean with biological replicates are shown with ± s.e.m.; n=3 biological replicates per condition; marker and color denote conversion TF cocktail used.

Fig. S5 Compact cocktail produces electrically active induced neurons at scale

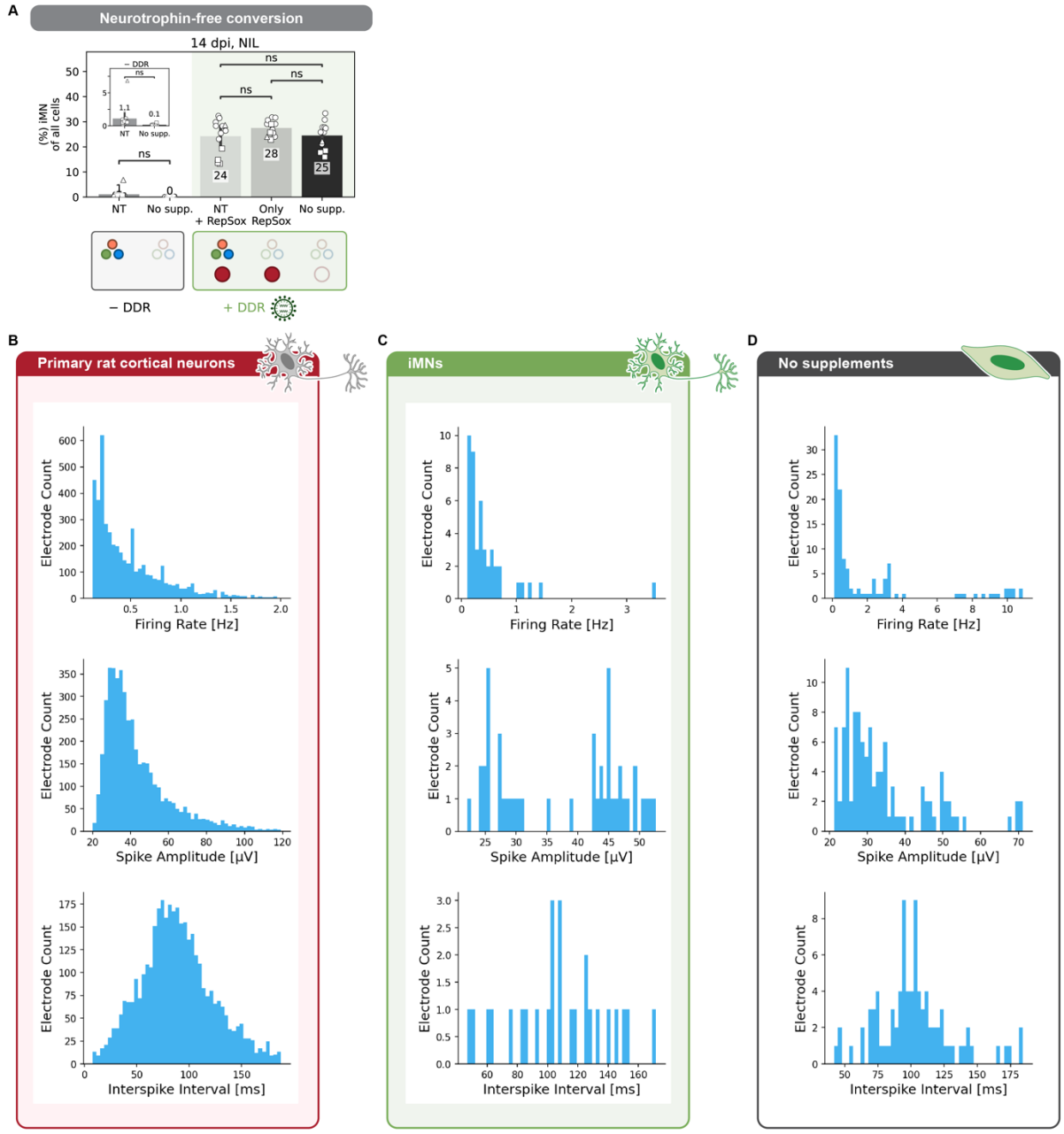

A. Conversion purity at 14 dpi for NIL ± DDRR. NIL infected cells were converted in N3 media ± neurotrophic growth factors (NT). NIL + DDRR infected cells were converted in N3 media with both NT and RepSox, with only RepSox, and with neither. Inset shows iMN purity for NIL (without DDRR) with zoom-in axis for clarity. Mean is shown with 95% confidence interval; marker styles denote biological reps; n = 3 biological reps per condition; One-tailed t-test with Bonferroni correction.

B-D. Histograms for the spontaneous electrical activity recorded in Fig. 3F-H. 35.54% of electrodes were active for the primary rat cortical neurons (left, red), 0.7% for the neurotrophins + RepSox iMNs (middle, green), and 1.73% for the no supplements (right, grey). n = 1 biological rep per condition

Significance summary: $p > 0.05$ (ns) and $*p \leq 0.05$

Fig. S6 Conversion cocktail and conditions influence the cell states of induced motor neurons

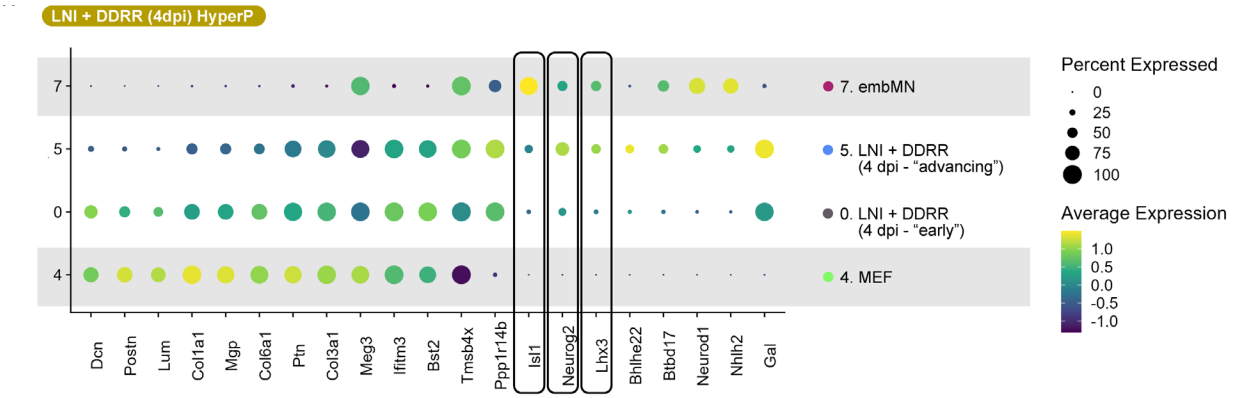

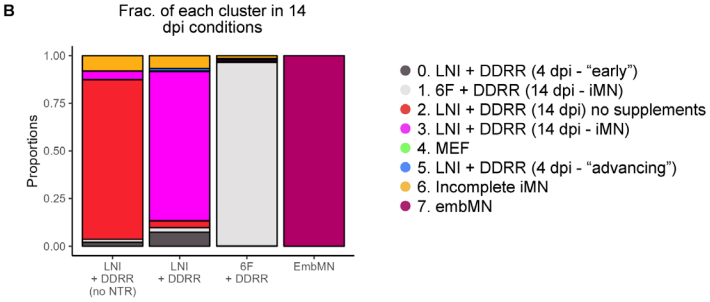

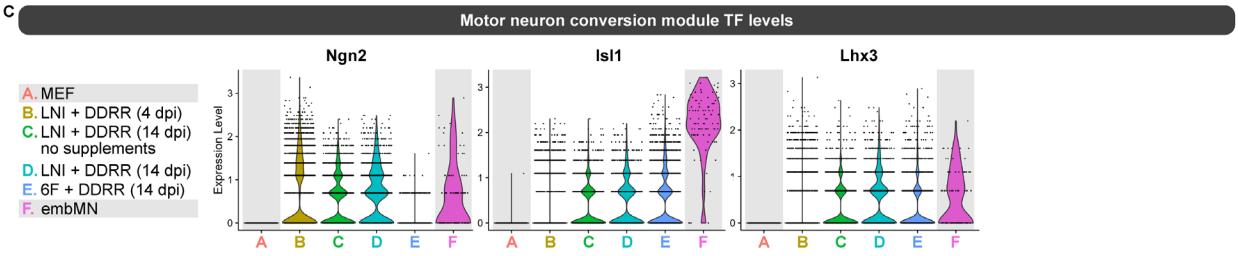

A. Feature plot for the 21 genes (top 20 marker genes and Isl1) differentiating the two major clusters in 4 dpi hyperP cells converted with LNI + DDRR. MEFs and embMN (clusters 4 and 7, respectively) are included as baselines. The iMN conversion factors (Ngn2, Isl1, Lhx3) are outlined with a box.

B. Distribution of embMNs and iMNs at 14 dpi across the 8 identified clusters (0-7) based on (Fig. 4C). Each library primarily maps to a single cluster.

C. Violin plots of expression across conversion conditions for the conversion TFs. Cells grouped in the incomplete iMN cluster (cluster 6) are removed from 14 dpi iMNs to allow comparison of fully converted cells.

Fig. S7 A compact cocktail generates engraftable neurons by direct conversion

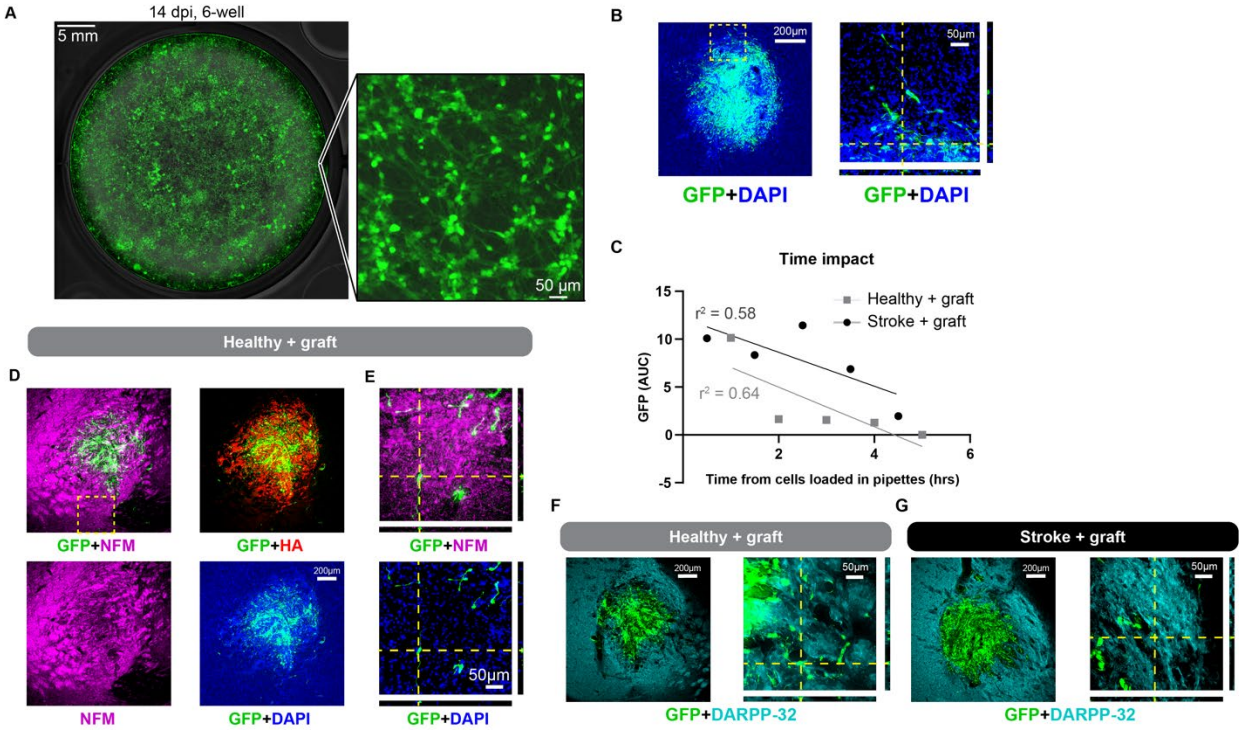

A. Image of converted iMNs in a 6-well at 14 dpi demonstrating that conversion induced with LNI + DDRR can scale with well-size. Phase contrast and Hb9::GFP overlaid, and an inset confirms neuronal morphology. Scale bar represents 5 mm in larger image and 50 µm in the smaller inset.

B. DAPI and GFP fluorescence for the striatal stroke lesion shown in Fig. 7B-D.

C. Correlation analysis of total GFP at 350 microns vs. time of graft relative to when cell grafts were loaded in pipettes with r^2 values for linear regression.

D-E. Coronal sections of healthy mouse striatum 2 weeks after converted iMN cell engraftment at various objectives. Sections were imaged for GFP, neurofilament (NFM), and NeuN.

F-G. Coronal sections of healthy (E) and stroke-induced (F) with grafted iMNs stained with striatal neuron marker (DARPP-32).